UNIVERSIDADE D
COIMBRA

António Sérgio Dias Morais

Desenvolvimento de um modelo computacional para o cancro da próstata

Dissertação no âmbito do Mestrado Integrado em Engenharia Biomédica orientada pelos Professores Doutores Rui Travasso e João Carvalho e apresentada ao Departamento de Física da Faculdade de Ciências e Tecnologias da Universidade de Coimbra.

Setembro de 2021

University of Coimbra

Integrated Master in Biomedical Engineering

Development of a Prostate Cancer Computational Model

António Sérgio Dias Morais

Thesis submitted to the Faculty of Sciences and Technology of the University of Coimbra in fulfillment of the requirements for the Master's Degree in Biomedical Engineering

Supervisors:

Ph.D. Rui Travasso

Ph.D. João Carvalho

UNIVERSIDADE D
COIMBRA

Coimbra, September 2021

Acknowledgements

Agradeço aos Professor Guillermo Lorenzo, Rui Travasso e João Carvalho por me orientarem e discutir comigo os resultados ao longo do desenvolvimento do modelo tal como oferecerem sugestões. Agradeço também aos membros do CFisUC pelas ideias e sugestões, nomeadamente, ao Marcos Gouveia pela ajuda com a implementaçao do modelo phase-field.

Não posso deixar de agradecer à minha família, que me ofereceram todo o apoio e comida caseira necessários para escrever uma tese.

Por último, mas não menos importante, agradeço à Vânia por me ensinar a usar Latex e me motivar.

Obrigado a todos!

Abstract

Prostate Cancer (PCa) is the second most frequent cancer in men. The limited individualization of the clinical management beyond risk-group definition has led to significant overtreatment and undertreatment rates, which may adversely impact the patients' lives and life expectancy, respectively. Thus, PCa is a paradigmatic condition in which an individualized predictive technology could make a crucial difference in clinical practice.

Mathematical modeling and computer simulation allow to better understand the mechanisms behind disease progression. The prostate is a small organ with an internal structure composed by a network of glands within smooth muscle connectivity tissue. To explore the role of prostate structure in PCa growth, two different mathematical models were developed. The first one, based on a 2D cellular Potts model, simulates the interactions between the different types of cells present on the prostate and the deformation of the glands as the tumor grows. The second model is a 3D phase-field model that takes into account tumor growth, prostate gland dynamics and nutrient consumption.

The phase-field simulations show how the tumor is able to develop a ramified phenotype in the tissue. The tumor was characterized on how much it deviates from a smooth morphology as a function of time and as a function of the underlying structure. The cellular Potts model gives important clues regarding how the cells and the glands rearrange locally on the early moments of tumor growth. These insights allow to study how the adaptation of the gland morphology as the tumor grows influences the lesion morphology.

We conclude that the internal ramified structure of the prostate has a determinant impact in the growth of the tumor. In particular, can be observed that it creates a path to spread at a faster rate and its deformations originate the observed Gleason Patterns.

Resumo

O cancro da próstata (PCa) é o segundo cancro mais frequente em homens. As características deste cancro tornam difícil individualizar o tratamento clínico, o que leva a uma grande percentagem de casos de subtratamento e sobretratamento, causando efeitos adversos na expectativa de vida e no dia-a-dia dos pacientes, respetivamente. Por isso, uma tecnologia preditiva pode causar uma diferença crucial no tratamento de PCa.

Modelos matemáticos e simulações computacionais permitem compreender os mecanismos que levam à progressão das doenças. A próstata é um órgão constituído por um conjunto de glândulas interconectadas num tecido muscular liso. Para explorar o papel desta estrutura no PCa, foram desenvolvidos 2 modelos matemáticos. O primeiro é baseado num Cellular Potts Model (CPM) a 2D, que simula a interação entre os diferentes tipos de células na próstata e a deformação causada pelo crescimento do tumor. O segundo é baseado num modelo phase-field a 3D que considera o crescimento do tumor, a estrutura das glândulas e o consumo de nutrientes.

As simulações do modelo phase-field mostram como o tumor desenvolve o fenótipo ramificado. O tumor foi caraterizado em quanto se desvia de uma morfologia esférica como função do tempo e da estrutura da próstata. O CPM permite observar importantes pistas sobre como as células e as glândulas se rearranjam localmente no inicio do desenvolvimento do PCa. Estes conhecimentos permitem estudar como a adaptação da morfologia das glândulas afeta a morfologia das lesões.

Concluímos que a estrutura ramificada da próstata tem um impacto significativo no crescimento do tumor. Em particular, pode-se observar que cria um caminho que permite o tumor espalhar-se da posição inicial mais rápido e que a deformação desta estrutura origina as lesões observadas nas biópsias.

Contents

List of Figures

List of Tables

Acronyms

BPH Benign Prostatic Hyperplasia. 5, 9

CPM Cellular Potts Model. v, ix, xi, 11, 12, 14, 28, 29, 47, 48

CSC Cancer Stem Cell. ix, 5, 17, 18, 25–28, 34–36, 47, 63

DRE digital rectal examination. 5

ECM Extra-Cellular Matrix. 11, 17, 18, 27, 30, 44, 57, 59–63

GP Gleason Patterns. iii, ix, 1, 6–8, 25, 32–36, 41, 43, 47, 48

GS Gleason Score. 6

H&E Haematoxylin and Eosin. 7, 41

ISUP International Society of Urologic Pathology. 6

MCS Monte Carlo Step. 14, 16, 18, 31

PCa Prostate Cancer. iii, v, 1, 5–7, 9, 17, 18, 20, 21, 23, 31–35, 40, 41, 47, 48

PDE Partial Differential Equations. 20, 22

PIN Prostatic intraepithelial neoplasia. 9

PSA prostatic-specific antigen. 4, 5

Chapter 1

Introduction

1.1 Objectives

This work is included in a project with the objective of creating a model capable of predicting the development of Prostate Cancer (PCa), to provide personalized treatment to patients and reduce over and under treatment. This thesis has the goal of creating PCa models to study the first stages of development of this tumor and the formation of the different Gleason Patterns.

1.2 Motivation

Prostate Cancer (PCa) is the second most common and the fifth more deathly cancer in men [1]. The large difference between the incidence and mortality is consequence of the death caused by PCa usually resulting from metastasis in other organs [2].

PCa screening reduced the number of deaths but, as a trade-off, increased the over treatment of this disease. This causes patients with lower grade PCa, that would not suffer any clinical consequences during their lifetime, to undergo the side effects of the treatment [3]. On the other hand, some patients with higher grade PCa do not receive the optimal treatment, which may cause the loss of several years of life [4].

To avoid under and over treatment, we should aim for a personalized diagnosis and treatment. If a patient-specific predictive model can be implemented, a optimal treatment can be chosen *in silico* to increase the quality of life of the patients.

To achieve such model, it is required to understand how the cancer growth causes the differences observed in the Gleason Patterns, to model cancer development and to predict how each parameter affects its growth.

Chapter 2

Biological Background

2.1 Prostate

The prostate is an organ of the male reproductive system. It is located under the bladder, surrounding the urethra (Figure 2.1). The weight of the prostate varies between 8.3±1.4g in young men to 10.9±3.4g in older men [5], and its size is comparable to a walnut for healthy prostates but can grow to the size of a tennis ball for men suffering from some diseases [6].

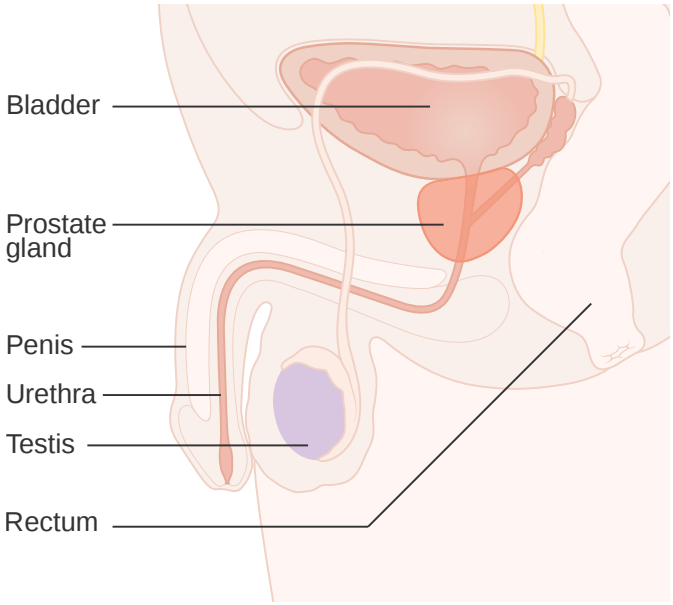

Figure 2.1: Diagram showing the position of the prostate.
Public Domain image by [7].

The prostate is responsible for the production of part of the fluids that compose the semen [8]. Prostatic secretions include zinc, citric acid, spermine, prostaglandins, cholesterol, seminin, acid

phosphatase, prostatic acid phosphatase, and prostatic-specific antigen (PSA) [9].

The prostate can be divided into an anterior fibromuscular stroma and 3 glandular zones, peripheral, central and transition zones. 70% of the glandular tissue is in the peripheral zone, 25% in the central zone, and 5% in the transition zone [8, 10, 11].

The contraction of the muscular tissue during orgasm secrets the prostate fluids into the prostatic urethra, through a ducts network [12], where it joins the sperm and fluids from the seminal vesicles. This contraction also closes the connection with the bladder preventing retrograde ejaculation [11].

The prostate is a tubuloalveolar exocrine gland [12, 13]. The glandular zones of the prostate can be separated in 2 parts, Stroma and Epithelium, separated by the basal membrane (Figure 2.2). The Stroma serves as support and is mainly constituted by connective tissue, fibroblasts and smooth muscle cells. There are 4 major types of cells on the Epithelium of the prostate: luminal cells, basal cells, stem cells and neuroendocrine cells [14, 15].

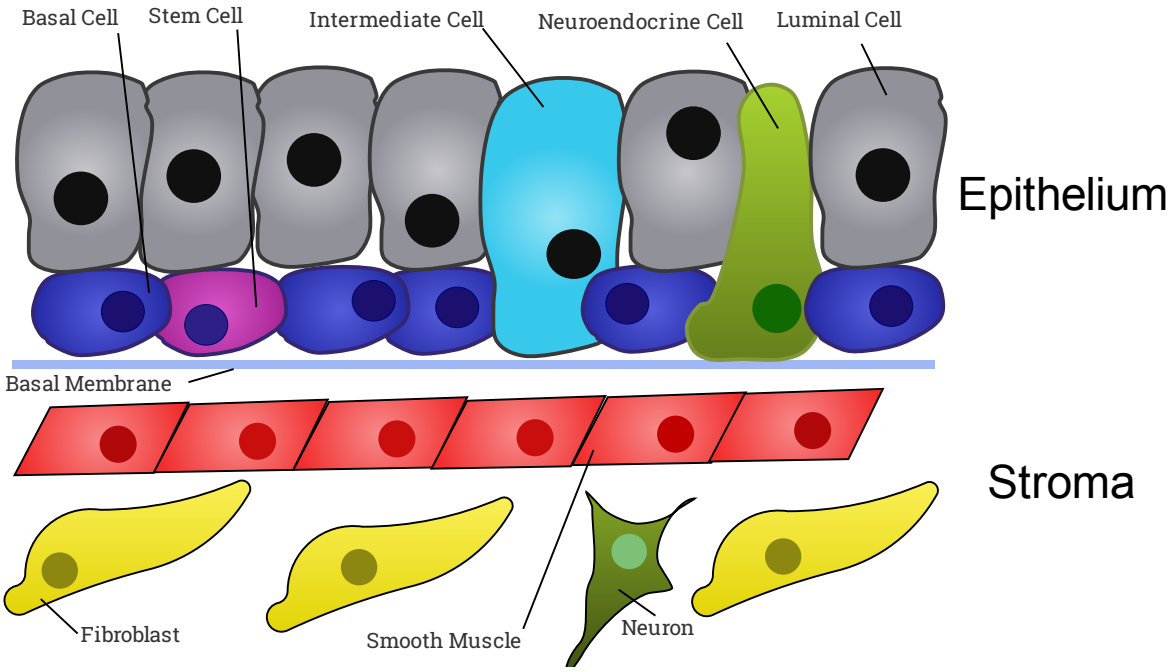

Figure 2.2: Cellular organization of the prostate gland.

The luminal and neuroendocrine cells are the only cell types capable of secretion [15]. Luminal cells are cuboid cells that form a pseudo-stratified layer. They are around 10 to 20 µm tall [15]. Basal cells are planar cells that form a layer between the luminal cells and the basal membrane [16]. Stem cells are responsible for cellular renovation and are found in the basal layer [16, 17]. Neuroendocrine cells regulate the secretions by autocrine and paracrine signaling

and are the less frequent type of cell [14].

In normal conditions, 1-2 % of the total prostatic cells die per day. This rate is compensated with an equally low rate of proliferation [18, 19]. In the epithelium some cells exist in an intermediate state between basal and luminal cells, expressing genes specific to each type [16,20].

There are 3 major diseases that affect the prostate. Prostatitis refers to several syndromes such as bacterial infections and inflammation [21]. Benign Prostatic Hyperplasia (BPH) is the non-malignant growth of the prostate associated with aging [22]. BPH is an enlargement of the gland due to cellular proliferation of prostatic stroma and epithelia [23]. The third disease is the prostate cancer. Usually, BPH is prominent in the transition zone [24] while 70% of all prostate cancers arise within the peripheral zone [11]

2.2 Prostate Cancer

Prostate Cancer (PCa) is the second most common and the fifth more deathly cancer in men [1]. This disease is mainly diagnosed in elder men with 85% of patients being diagnosed after the age of 65 [25]. Most men diagnosed with PCado not die from this disease. Death caused by PCa usually results from metastasis in other organs [2].

2.2.1 Origin

There is some controversy around the cellular origin of PCa. Normally, PCa is a luminal-like adenocarcinoma (95% of the prostate tumors) [24, 26]. This supports the idea that the tumor cells deriving from differentiated luminal cells [27].

However some *in vitro* studies revealed that only the cells phenotypical identical to stem cells could self-renew and, if conditions for differentiation appear, luminal cells would be found [28]. This hypothesis defines two groups of cells in the tumor: one that can self-renew, Cancer Stem Cell (CSC), and differentiated epithelial cells without proliferative ativity [28–31].

2.2.2 Diagnosis

PCa is a type of cancer that only causes symptoms in advanced stages, making screening an important tool to figth the disease [32]. Earlier, the digital rectal examination (DRE) was the main method for screening. However, DRE has a large inter-examiner variability, and detects PCa at an advance stage [33]. Nowadays, the most frequent screening methods are DRE and PSA testing. PSA is a protein produced in the prostate epithelium and secreted to the lumen,

being a major part of the semen (0.5 to 2 ng/mL). This protein can be found in several forms on the blood (pro-PSA, BPSA's, free-PSA) and semen, and the comparative levels of these forms are affected by the different prostate pathologies [34].

The use of new methods for screening has reduced the deaths from PCa but lead to an increase in over-treatment, which has side effects in the patients quality of life [3].

2.2.3 Gleason Score

The Gleason Score (GS) is used to grade PCa [35]. This system requires the observation under microscope of the prostate tissue obtained via biopsy, and is a good predictor of survival [36]. Table 2.1 and Figure 2.3 give a brief description and illustration of the Gleason Patterns (GP).

Table 2.1: Brief description of the Gleason Patterns. From [35]. More detail in [37, 38].

Grade	Description
1	Simple round glands, close-packed in rounded masses with well-defined edges
2	Simple rounded glands, loosely packed in vague, rounded masses with loosely defined edges
3A	Medium sized single glands of irregular shape and irregular spacing with ill-defined infiltrating edges
3B	Very similar to 3A, but small to very small glands, which must not form significant chains or cords
3C	Papillary and cribriform epithelium in smooth, rounded cylinders and masses; no necrosis
4A	Small, medium, or large glands fused into cords, chains, or ragged, infiltrating masses
4B	Very similar to 4A, but with many large clear cells, sometimes resembling "hypernephroma"
5A	Papillary and cribriform epithelium in smooth, rounded masses, more solid than 3C and with central necrosis
5B	Anaplastic adenocarcinoma in ragged sheets

These patterns are used to grade the tumor and calculate the GS. Patients may have tumors with different GP in different zones. The GS of a patient is obtained by the sum of the most predominant (primary) and the second most predominant (secondary) patterns found on the biopsy's sample. If there is a third, higher grade, pattern in a needle biopsy it is recommended, by the 2005 International Society of Urologic Pathology (ISUP) Consensus, to use it as the secondary pattern instead [40, 41].

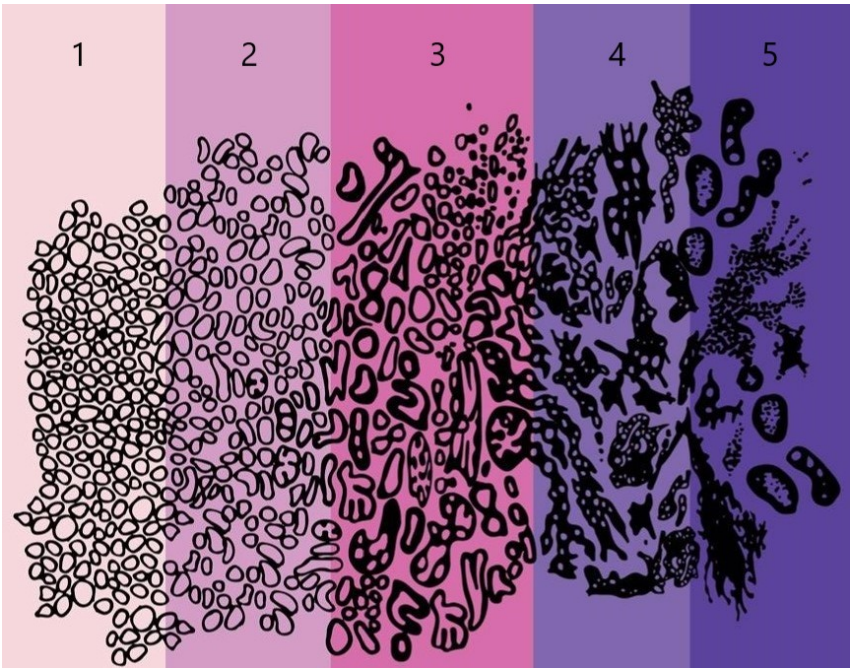

Figure 2.3: Gleason Patterns. Adapted from [39].

3D Structure

The GP are a consequence of the changes in the tuboloalveolar structure of the prostate due to PCa [42]. Some lesions of the prostate can cause the same patterns in Haematoxylin and Eosin (H&E) slides but have a different 3D architecture [43]. The 3D architecture of the prostate is being studied to assist in PCa diagnosis and increase their accuracy [42–48].

Leenders *et al* [42] describes the 3D architecture associated to each Gleason Patterns (Figure 2.4). GP3 has tubules with local interconnections and is continuous in space to Poorly Formed GP4 and Fused GP4. In Fused GP4 tubule interconnections often occur at distances smaller than the tubular diameter. In Poorly Formed GP4 the tubular size and lumen diameter are smaller, and the interconnections more frequent than GP3. Single cells and Cords GP5 are continuous in space with Poorly Formed glands, were lumen size further decreased until lumens disappear. Cribriform GP4 and Solid GP5 with or without comedonecrosis consist of serpentine fields of epithelial cells. These two patterns form a continuous structure with or without the presence of recognisable inter-cellular lumens. Glomeruloid GP4 represent intraluminal protrusions of epithelial cells appearing within a background of GP3 tubules, that are mostly present at the sites of tubular interconnections. This last structure can be considered as an intermediate state between the two groups of structures that form a spacial continuum. The first group being defined by the contact with the stroma with different gland diameters, lumen size and number

of interconnections (GP3, Poorly Formed and Fused GP4 and Single cells and Cord GP5). And the second group of structures being defined by the majority of cells not being in contact with the stroma (Cribriform GP4 and Solid GP5).

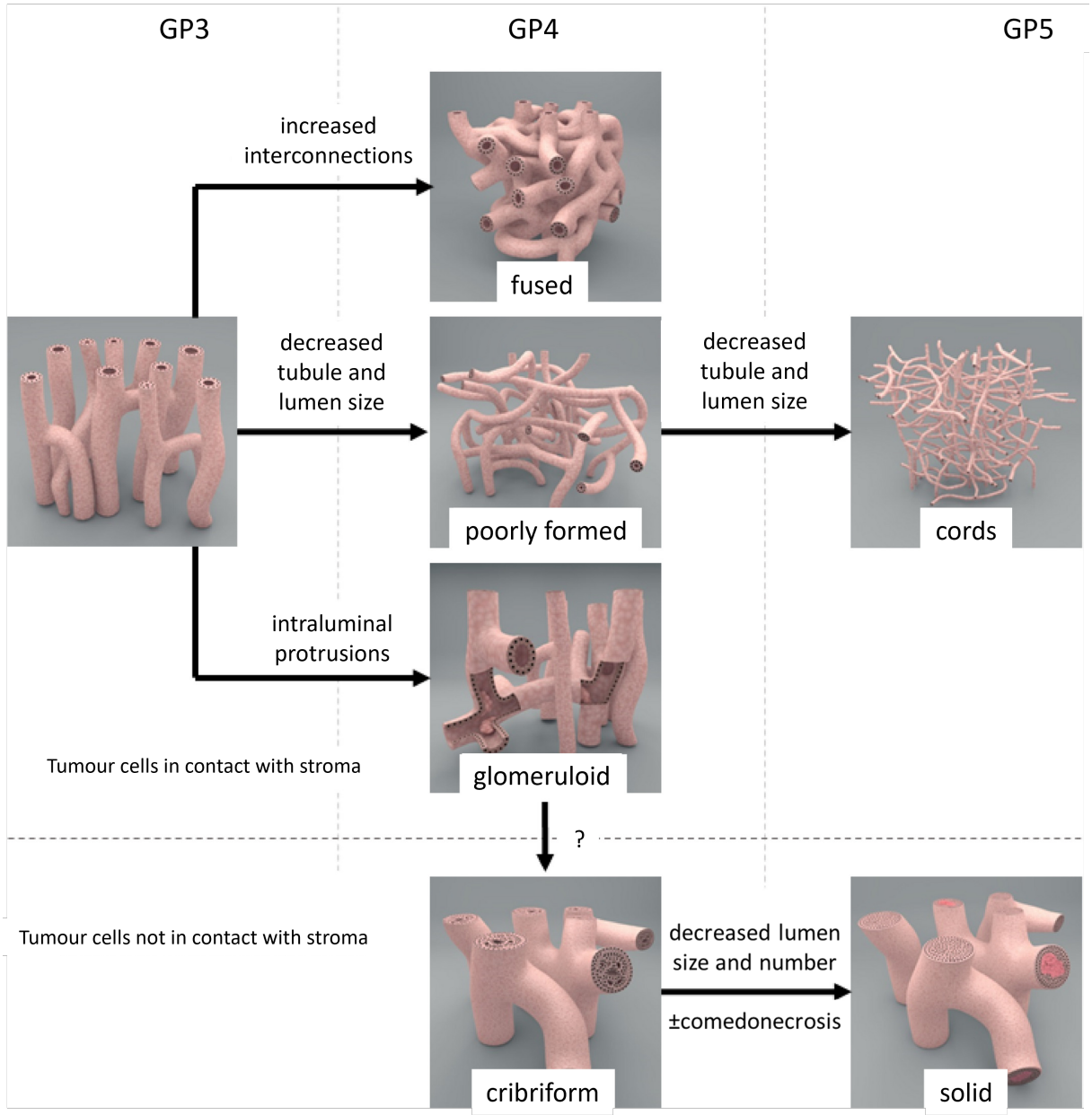

Figure 2.4: Schematic overview of the Gleason growth patterns in prostate cancer. Three-dimensionally, two morphological subgroups of growth pattern are observed. Gleason pattern 3, poorly formed and fused Gleason pattern 4 and Gleason pattern 5 cords form the first subgroup, in which the vast majority of the tumour cells make direct contact with the surrounding stroma. The second subgroup consists of cribriform Gleason pattern 4 and solid Gleason pattern 5; the vast majority of tumour cells do not make contact with the surrounding stroma. Comedonecrosis might be present in this subgroup. Glomeruloid structures represent a morphological intermediate pattern between the two subgroups. From [42].

2.2.4 PCa and other diseases

Prostatic intraepithelial neoplasia (PIN) is a type of prostate lesion considered to be a precursor of invasive PCa. At least 30% of the patients with high-grade PIN developed PCa within 1 year [49]. However, the causality between PIN and invasive PCa is still subject of debate [24, 50].

Patients that suffer from BPH have a higher risk of developing PCa [51]. However, statistical and *in silico* studies suggest that larger prostates have a protective effect against the malignancy of PCa [52–54]. As large prostates have less aggressive tumors than smaller prostates, patients with BPH have less dangerous PCa.

Chapter 3

Methods

3.1 Cellular Potts Model

A Cellular Potts Model (CPM), also known as the Glazier-Graner-Hogeweg model, is a computational approach to model irregular and highly fluctuating cell shapes [55]. It has a high resolution when compared to other methods, such as vertex or cellular automata models [56]. Moreover, the CPM is described by energies unlike most models that are described by forces.

The CPM was originally used to simulate cell sorting [57]. Cell sorting is achieved by the CPM ability to replicate cell to cell differential adhesion and cells interactions, aggregation and desegregation. Furthermore, this model is also capable to simulate tissue growth, cell division and cell signalling. This allows the study of tissue morphogenesis [58] and cell migration [59]. All these capabilities concede CPM the ability to study tumor growth, tumor evolution and tumor invasion [60].

The domain of simulation is represented by a grid with elements (Figure 3.1). The CPM was created to simulate a biological systems, so, the distinct elements of the simulation will usually correspond to parts of cells [61], cells or groups of cells, but they can also be empty spaces like Lumens, a void like a cut, an obstacle like an implant [62], or anything else properly modelled. By convention, the element with ID 0, is used to simulate the medium around the cells, for instance the Extra-Cellular Matrix (ECM) in *in vivo* conditions, or plastic or glass in *in vitro*.

In biological systems, different cells can be of the same type if they share the same characteristics. The elements will be grouped in types that possess certain properties. These properties define the energy, behavior (e.g. mitosis and differentiation) and interaction with other elements. Each element can occupy several pixels on the grid, but each pixel can only be occupied by one element, identified by the element ID.

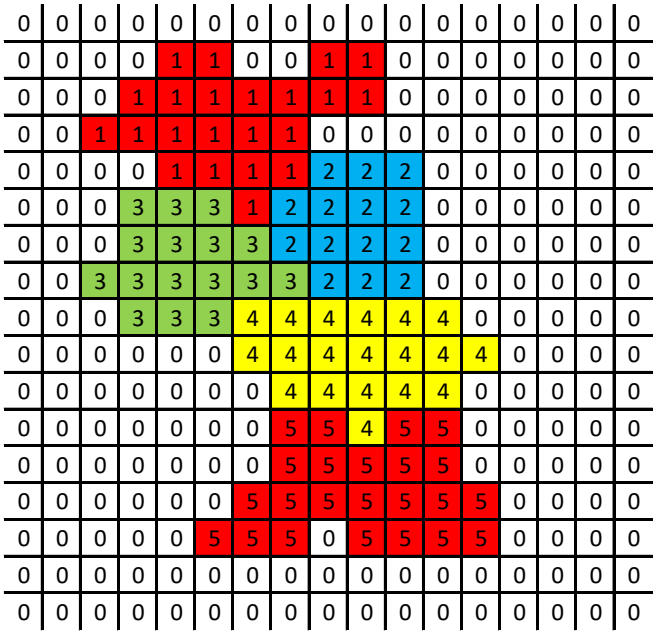

Figure 3.1: Example of a CPM representation. The grid squares represent the pixels, the numbers represent the cell that occupies the pixel and the color represents the type of each cell.

Let us define the required formalism to make the equations as clear as possible. CPM is build over a grid of pixels, each pixel is occupied by one and only one cell and cells have types (See Figure 3.1 for a visual example). Let us consider that:

- p_{ij} is the pixel with position (i, j) on the 2D grid;
- $E(p_{ij}) \equiv E_{ij}$ is the element that occupies the pixel p_{ij};
- E_X is the element with ID X ($X = 0, 1, 2, ...$, as many as the number of cells in the domain);
- $\tau(E_X) \equiv \tau_X$ is the type of the element X ($\tau_X = 0, 1, 2, ...$, as many as the types of cells in the system).

This computational implementation of CPM used in this work was adapted from the code introduced in Carvalho *et al.* [63], written in C++ and used to study the development of bladder tumors.

3.1.1 Hamiltonian

This type of model represents, over time, a system evolving to the state that minimizes an energy function, the Hamiltonian. The CPM is not based on the forces exerted by the elements; instead, the Hamiltonian is associated with the shape of the elements in the model

and their interactions (e.g. adhesion). Equation (3.1) shows the Hamiltonian corresponding to one Element:

$$\begin{aligned} H &= \sum_{E} H(E) \\ H(E) &= H_{shape}(E) + H_{adh}(E) \end{aligned} \tag{3.1}$$

where $H_{shape}(E)$ increases with the deviation from the target shape of the element E, and $H_{adh}(E)$ is the adhesion energy of the interfaces between the element E and its neighbors. Other terms can be added to simulate other processes, such as chemotaxis [64]. The adhesion energies are defined between the types of elements.

In the model, the energy associated with the interface between one pixel (p_{ij}) and its neighbors is given by:

$$H_{adh}(p_{ij}) = \sum_{k=i-1}^{i+1} \sum_{l=j-1}^{j+1} J\Big(\tau(E_{ij}), \tau(E_{kl})\Big) \times \big(1 - \delta_{E_{ij}E_{kl}}\big) \tag{3.2}$$

where $J\big(\tau(E_{ij}), \tau(E_{kl})\big)$ is the adhesion energy between the types of the elements that occupy the positions (i, j) and (k, l). $\delta_{E_{ij}E_{kl}}$ is the Kronecker delta, meaning, if both positions are occupied by the same element then $\delta_{E_{ij}E_{kl}} = 1$.

J is an user defined symmetric matrix, where each row and column corresponds to one type of cells, and $J_{ij} = J_{ji}$ is the energy of the interface between cells of type i and j.

When calculating the contribution of $p_{ik},\ k = j + 1$ the interface between p_{ij} and p_{ik} will be added again. Therefore, by the definition, the energy associated with the interface between elements is half the sum of the individual pixels contribution:

$$H_{adh} = \frac{1}{2} \sum_{i,\ j} H_{adh}(p_{ij}) \tag{3.3}$$

Two measurements of shape have been considered, the Area and the Length of each cell. The energy associated with each measure increases with the deviation from the expected value for each cell:

$$H_{area}(E_X) = \lambda_{a\,\tau_X} \left(\frac{A(E_X) - A_{\tau_X}}{A_{\tau_X}} \right)^2 \tag{3.4}$$

$$H_{len}(E_X) = \lambda_{l\,\tau_X} \left(\frac{L(E_X) - L_{\tau_X}}{L_{\tau_X}} \right)^2 \tag{3.5}$$

where $A(E_X)$ and $L(E_X)$ are, respectively the area and length of element X, one element (cell) on the model; $\lambda_{a\,\tau_X}$ and $\lambda_{l\,\tau_X}$ are the weights associated with the type of element X; and A_{τ_X}

and L_{τ_X} are the target area and length for the type of element X. These parameters are user defined. The area of a cell is defined as the number of pixels it occupies:

$$A(E_X) = \sum_{p,\ E(p)=E_X} 1 \tag{3.6}$$

The length is the larger distance between any two pixels occupied by the same element:

$$L(E_X) = \max_{\substack{i,\ j,\ k,\ l \\ E(p_{ij})=E_X \\ E(p_{kl})=E_X}} \left(\sqrt{(i-k)^2 + (j-l)^2}\right) \tag{3.7}$$

To run a Cellular Potts Model (CPM), one must calculate the probability for the state to change. This probability depends on the variation of the Hamiltonian ($\Delta H = H^1 - H^0$) between an alternative state (H^1) and the current state (H^0).

$$Probability(H^0 \to H^1) = \begin{cases} 1, & \Delta H \leq 0 \\ e^{-\frac{\Delta H}{T}}, & \Delta H > 0 \end{cases} \tag{3.8}$$

where T is a parameter adjustable to allow greater variations of energy (it can be used to describe the degree of fluctuation of the cellular membranes). If the energy decreases ($\Delta H \leq 0$), the alternative state becomes the new state; if the energy increases ($\Delta H > 0$), the state may change to the alternative state or remain the same.

The Hamiltonian difference between states used in Equation (3.8) is given by:

$$\Delta H = \Delta H_{adh} + \Delta H_{area} + \Delta H_{len} \tag{3.9}$$

Because on each iteration of the MCS only one random pixel can change, p_{ij}, the adhesion energy without p_{ij} contribution is the same in both states. So, we can simplify the adhesion

term:

$$
\begin{aligned}
\Delta H_{adh} &= H^1_{adh} - H^0_{adh} \\
&\quad \text{(by expansion of Eq. (3.2))} \\
&= \overbrace{H^1_{adh} - H^1_{adh}(p_{ij})}^{H_{adh} \text{ w/o } p_{ij} \text{ contrib.}} + \underbrace{H^1_{adh}(p_{ij})}_{p_{ij} \text{ contrib.}} - \left(\overbrace{H^0_{adh} - H^0_{adh}(p_{ij})}^{H_{adh} \text{ w/o } p_{ij} \text{ contrib.}} + \underbrace{H^0_{adh}(p_{ij})}_{p_{ij} \text{ contrib.}} \right) \\
&\quad \left(H^1_{adh} - H^1_{adh}(p_{ij}) \quad = \quad H^0_{adh} - H^0_{adh}(p_{ij}) \right) \\
&= H^1_{adh}(p_{ij}) - H^0_{adh}(p_{ij})
\end{aligned}
\tag{3.10}
$$

By changing the element that occupies the changing pixel, we alter the area and length of 2 elements, the one that occupies the pixel in state 0, E_X, and the one that occupies the pixel in state 1, E_Y. If $A(E_X) \equiv A^0(E_X)$ is the volume of element X in state 0, $A^1(E_X) = A^0(E_X) - 1$ is the area in state 1 of E_X, similarly, $A^1(E_Y) = A^0(E_Y) + 1$, is the area of E_Y in state 1. From Equation (3.4) we can calculate ΔH_{area} as a function of the current cell areas (at state 0):

$$
\begin{aligned}
\Delta H_{area} &= \Delta H_{area}(E_X) + \Delta H_{area}(E_Y) \\
&= H^1_{area}(E_X) - H^0_{area}(E_X) + H^1_{area}(E_Y) - H^0_{area}(E_Y) \\
&\quad \big(A(E_X) \equiv A^0(E_X),\ A(E_Y) \equiv A^0(E_Y) \big) \\
&= \lambda_{a\,\tau_X} \left(\frac{A(E_X) - 1 - A_{\tau_X}}{A_{\tau_X}} \right)^2 - \lambda_{a\,\tau_X} \left(\frac{A(E_X) - A_{\tau_X}}{A_{\tau_X}} \right)^2 + \\
&\quad + \lambda_{a\,\tau_Y} \left(\frac{A(E_Y) + 1 - A_{\tau_Y}}{A_{\tau_Y}} \right)^2 - \lambda_{a\,\tau_Y} \left(\frac{A(E_Y) - A_{\tau_Y}}{A_{\tau_Y}} \right)^2
\end{aligned}
\tag{3.11}
$$

$$
\Delta H_{area} = \lambda_{a\,\tau_X} \frac{1 - 2\big(A(E_X) - A_{\tau_X}\big)}{A^2_{\tau_X}} + \lambda_{a\,\tau_Y} \frac{1 + 2\big(A(E_Y) - A_{\tau_Y}\big)}{A^2_{\tau_Y}}
$$

By the definition given to the length of a cell it is not possible to know the relation of lengths for each state *a priori*, therefore, the expression to calculate ΔH_{len} cannot be further simplified. But the length, on Equation (3.7), can be rewritten for computational speed proposes. If T_X and S_X are the set of all pixels occupied by the area of the cell X and the subset of pixels in the surface, in contact with other cells, respectively. The search of the maximum distance can

be limited the points of the subset S_A.

$$L(E_X) = \sqrt{\max_{\substack{i,\ j,\ k,\ l \\ p_{ij}, p_{kl} \in S_X}} \left((i-k)^2 + (j-l)^2 \right)} \tag{3.12}$$

Computationally, this reduces the pairs of points to search the maximum from $\binom{T_X}{2}$ to $\binom{S_X}{2}$ combinations, where $S_X \subsetneqq T_X$.

3.1.2 Time Step

Each time step has 2 parts. One is the Monte Carlo Step (MCS), constituted by several iterations where an element can move 1 random pixel inward or outward in any point of its boundary.

The MCS has as many iterations as there are pixels in the grid. In each iteration one pixel and one of its neighbors are randomly chosen and it is calculated the probability to change the element that occupies the first pixel to the element that occupies the second. In each iteration, the following steps are taken:

Step 1. One random pixel is chosen, $p_1 = p_{ij}$;

Step 2. One neighbor pixel is chosen randomly, $p_2 = p_{kl}$,
$k \in \{i-1, i, i+1\},\ l \in \{j-1, j, j+1\},\ p_{kl} \neq p_{ij}$;

Step 3. Check the elements in the chosen pixels:

(a) If they belong to the same element, $E(p_1) = E(p_2)$

- Stop iteration and start next iteration from Step 1.

(b) Otherwise

- Continue to Step 4.

Step 4. Calculate the probability to change state (according to Equation (3.8)) by making the element in p_1 change to the element in p_2;

Step 5. Accept that change with the probability calculated in Step 4.

The other part of the time step is dependent on the characteristics added to the model. The model in the present work updates the elements' time of proliferation, kill cells randomly according with user defined probabilities, causes cellular proliferation and cellular differentiation. The model characteristics are explained further in subsection 3.1.4.

3.1.3 Types of Cells

Each cell (element) has a well defined type with specific characteristics. Many cells can be of the same type, but each cell only as one type (that can change in time in the case of cellular differentiation).

In the present model, besides defining the adhesion energy of the interfaces between the cells, the type of cell defines the expected cell area and length. The type also defines the behavior described in subsection 3.1.4.
Seven types of elements have been created to simulate the prostate structures and PCa growth:

0. Extra-Cellular Matrix (ECM)
1. Stroma
2. Basal Cell
3. Stem Cell
4. Luminal Cell
5. Lumen
6. Tumor Cell
7. Cancer Stem Cell (CSC)

As mentioned before, the simulation grid has a default cell type. On this model, the default corresponds to the *ECM*, the support matrix of biological tissues.

Basal, *Stem* and *Luminal* cells represent different types of cells in the prostate epithelium (see section 2.1). Neuroendocrine cells are very rare [65] and have not been simulated.

Stroma is a special element that represents the group of cells and fibers that constitute it. The *Stroma* can also simulate the basal membrane by adjusting its rigidity and adhesion with the other types of cells, namely the *Basal* and *Stem* cells.

The *Lumen* is another special element that creates on the model the natural tendency of the prostate cells to form ducts. Because it simulates an empty space, it has more loosened parameters than other types of cells.

The *Tumor* cell type, like *Stem* cells, can suffer mitosis. However, *Tumor* cells have random and more frequent proliferation.

Cancer Stem Cell (CSC) is a special type created to recreate the formation of new interconnections of ducts in PCa. Like a *Stem* cell, *CSC* can divide and originate 2 different types of cells, and, like a *Tumor* cell, has a random, uncontrolled and frequent proliferation. A more detailed explanation about this type of cells can be found in chapter 4.

Stem, *Tumor* and *CSC* cells have the ability to proliferate by mitosis. Depending on the type, the daughter cells may be of different types. Mitosis is important for the implementation of homeostasis in the model, explained in the next subsection.

3.1.4 Homeostasis

A biological system is in constant change, mainly due to cellular movement, death and proliferation. The cellular movement is guaranteed by the Hamiltonian during the MCS. Death, mitosis and differentiation are implemented outside the Hamiltonian.

In normal conditions, cellular death, or apoptosis, can be modeled as a random process dependent on the type of cell. The model allows to treat the probability of death of a certain cell type as a user-defined parameter. If a cell dies the area it occupies turns into *ECM*.

Mitosis is a very important part of tumor progression and cellular renovation. Not all types of cells have the ability to divide and even the ones who have can be limited by their size. This model defines a mitosis area ($A_{mitosis}$) to take in account this limitation. Other limitation to mitosis is the cell lifetime. The model considers for each cell the *time of proliferation* to model this limitation. Only *Tumor*, *Stem* and *CSC* cells can undergo mitosis. Depending on the mother's type, the daughter cells can be of the same type or of different types. A *Stem* cell will originate one *Stem* cell and one *Basal* cell, while a *Tumor* cell will originate two *Tumor* cells and a *CSC* originates one *CSC* and one of these 4 types, with adjustable probabilities. The division is always chosen to create cells of similar size.

Mitosis can divide a cell along any plane or, if the cell has polarization, it can divide the cell in such a way to maintain polarization. The model considers both types of mitosis with the introduction of the Rule 9 of Rule Sets #3 and #4 (Table 4.3).

Cell polarization is defined by the cells' different internal structures dependent of the contacts with neighbor cells. Luminal epithelium cells tend to have a high polarization, its internal structure allows to secrete into the lumen and not into the basal layer. This polarization can affect the mitosis of a cell. Therefore, a cell with polarization can divide in order for the daughter cells to stay in contact with the same types of cells as the mother. A cell polarization is defined by the contacts it makes, based on the types of cells of the layers in contact with its own. This

is, a cell of the luminal layer (*Luminal* and *Tumor*) has polarization if is in contact with the *Lumen* and a cell of the basal layer (*Stem* and *Basal*). A cell of the basal layer must be in contact with *Stroma* and the epithelium layer to have polarization.

Differentiation is the capacity for a cell to change its type. When a cell originates, by mitosis, cells of different types, one of them has actually differentiated. However, for the definition of the Rules in Table 4.3, explained in subsection 4.1.1, allows to consider that type of differentiation a part of mitosis, and distinguishable from differentiation without mitosis. As cells move and change the contacts with their neighbors they can change their phenotype and change cell type. The model considers contact with certain types of cells the trigger to change type. The types of contacts that function as triggers for each type of cell are described in Table 4.3.

3.2 Phase-Field Model

Phase-field models were developed in physics to study non-equilibrium systems and have been used to describe several material phenomena [66]. The phase-field models a microstructure without the need to track the evolution of individual interfaces [67]. To do this, the state of the entire system is represented by a continuous variable, the order parameter ϕ (Figure 3.2).

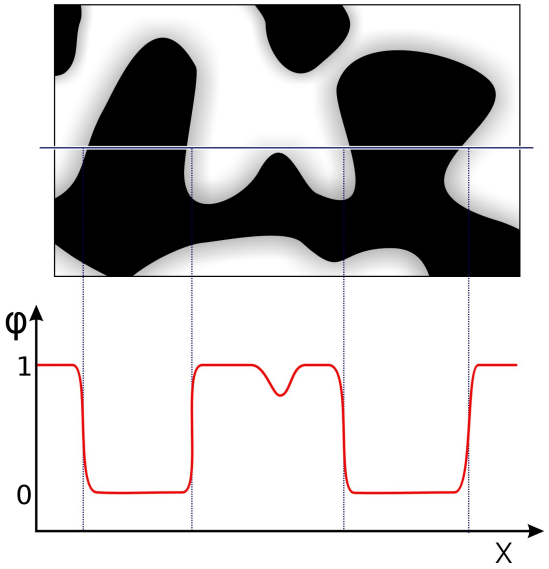

Figure 3.2: Schematic illustration of a two phase microstructure in phase-field simulations. The order parameter (ϕ) profile is shown on a line across the domain. Gradual change of order parameter from one phase to another shows the diffuse nature of the interface.

The order parameter ϕ takes the value of 1 to represent the tumor and the value of 0 to represent the healthy tissue. Where ϕ is between 0 and 1, is the interface between the two

phases.

$$\phi = \begin{cases} 1, & tumor \\ 0, & healthy \end{cases} \tag{3.13}$$

It's also common to see ϕ taking the values of 1 and -1 for tumor and healthy tissue, respectively [66, 68, 69].

The phase-field method describes problems with moving interfaces, using Partial Differential Equations (PDE) in a fixed domain [70]. There are methods to enhance accuracy and speed of Phase-field models, like solving PDEs in the complex domain without mesh generation [70].

The basic model is easily adaptable to different problems, and has already been applied to PCa [52, 71–73].

3.2.1 Mathematical Approach

The model from Lorenzo *et al.* [72] was adapted, and implemented with different speed enhancements. Their model was used to study the PCa development on the full prostate volume based on medical images of individual patients.

Tumor

Equation (3.14) models the tumor and healthy tissue interaction in the phase-field model as a diffusion-reaction model. The model must allow the tumor to diffuse (invade healthy tissue), proliferate and die.

$$\frac{\partial \phi}{\partial t} = \lambda \nabla^2 \phi - \frac{1}{\tau} \frac{dF(\phi)}{d\phi} + \chi \sigma \phi - A\phi \tag{3.14}$$

where the first two terms on the right hand side represents the diffusion of the tumor, χ is the proliferation of tumor in the presence of nutrient (σ) and A is the apoptosis of the tumor. $F(\phi)$ is a double well function with two equal potential minimums at 0 and 1 (Equation (3.15)). This function allows the coexistence of tumor and healthy tissue with a diffuse interface between them.

$$F(\phi) = 16\left(\phi^4 - 2\phi^3 + \phi^2\right) \Rightarrow \frac{dF(\phi)}{d\phi} = 64\phi(\phi - 1)\left(\phi - \frac{1}{2}\right) \tag{3.15}$$

In Equation (3.14), there is a difference from Lorenzo *et al.*'s model [72]. The third term original form, $\chi\sigma$, was adapted to only allow proliferation where there is tumor, by the multiplication by ϕ.

Nutrient

A tumor to grow requires resources such as oxygen, glucose and amino acids. All these resources come from the same source, the blood, and are diffused through the tissue. For simplicity and speed, they can be combined and simulated as one single compound, the nutrients (σ). The nutrients are not equally available in space, because vessels do not cover all points in the tissue and because cells consume nutrients. To model the local fluctuations in the supply of nutrients, its considered a nutrient source term on he form $s = s_0 + \eta$ where η is a small random fluctuation. This fluctuation is coarse grained, thus being set constant in small cubes with an adjustable edge. This results in a better stability when integrating.

The nutrients concentration will be affected by the tumor, the source and its diffusion and degradation:

$$\frac{\partial \sigma}{\partial t} = \epsilon \nabla^2 \, \sigma + s - \delta\phi - \gamma\sigma \tag{3.16}$$

where ϵ is the diffusion coefficient, s represents the source term, δ is the consumption by the tumor (ϕ), and γ is the degradation/consumption of nutrient in normal conditions.

Because it simulates the development of the tumor, the source (s) is considered to be constant in time and initially σ is set equal to s.

Ducts

To study the influence of the prostate ductal structure in PCa, it is necessary to create a new order parameter dependent on the morphology, θ. Therefore, θ represents the tissue and is defined as:

$$\theta = \begin{cases} 1, & tissue \\ 0, & ducts \end{cases} \tag{3.17}$$

Including a new term dependent on θ in Equation (3.14), the simulated PCa development becomes influenced by the micro structure of the prostate. The method to introduce this influence in the model was one of the studies of this work and the results can be seen in subsection 4.2.2

3.2.2 Simulation Time

A major concern when employing a mathematical model is the time to run the simulation. To do computational integration, it is required for the time step to be under a certain value, above which, the model may became numerical unstable.

There are several ways to reduce the runtime of the simulations. The easiest one is to reduce the complexity or the size of the system. Other ones use more fitting algorithms to solve the mathematical equations.

In this work two methods were used to reduce the runtime: an approximation that simplified the model and the use of implicit and semi-implicit methods that allow to use a longer time step.

Simplification

Because the nutrient diffusion is much faster than the tumor dynamics, $\epsilon \gg \lambda$, one can assume the nutrient to be in a stationary state in the time scale used to study the tumor development. Therefore, from Equation (3.16):

$$\frac{\partial \sigma}{\partial t} = \epsilon \nabla^2 \sigma + s - \delta\phi - \gamma\sigma \approx 0 \tag{3.18}$$

This assumption allows to increase the time step that would be limited by the nutrient diffusion. As σ is dependent of ϕ, it is calculated every iteration to find its new stationary state.

Implicit and semi-implicit methods

Implicit methods have higher numerical stability than explicit methods. Fourier transforms can be used to treat PDE problems with periodic boundary conditions. When comparing to finite differences methods, Fourier Transforms (using Fast Fourier Transform algorithms) have lower computational cost to calculate the second order derivatives present in the model.

To calculate the laplacian of ϕ in Equation (3.14):

$$\lambda\nabla^2\phi = \mathscr{F}^{-1}\left\{\mathscr{F}\left\{\lambda\nabla^2\phi\right\}\right\} = \mathscr{F}^{-1}\left\{-\lambda k^2 \phi^{(k)}\right\} = \lambda\mathscr{F}^{-1}\left\{-k^2\phi^{(k)}\right\} \tag{3.19}$$

From Equation (3.18), in the Fourier space, comes:

$$\begin{aligned}\mathscr{F}\left\{\epsilon\nabla^2\sigma + s - \delta\phi - \gamma\sigma\right\} = \mathscr{F}\{0\} \;\Leftrightarrow -\epsilon k^2\sigma^{(k)} + s^{(k)} - \delta\sigma^{(k)} - \gamma\phi^{(k)} = 0 \Leftrightarrow \\ \Leftrightarrow \sigma^{(k)} = \frac{s^{(k)} - \gamma\phi^{(k)}}{\epsilon k^2 + \delta} \;\Leftrightarrow \sigma = \mathscr{F}^{-1}\left\{\frac{s^{(k)} - \gamma\phi^{(k)}}{\epsilon k^2 + \delta}\right\}\end{aligned} \tag{3.20}$$

Because s is constant during all the simulation, to calculate σ it is only required to use the previously calculated transform of ϕ to advance in the simulation.

3.2.3 Observables

As PCa grows, it forms non-spherical structures. If assumed that these structures are deformations from a sphere, several observables can be used to evaluate this deviation during the simulation progression. To complement the information from this observables, the volume of the tumor has also been considered.

Volume

ϕ represents the tumor in each point of the grid, so, the volume of the tumor can be calculated by:

$$Volume = \Delta x \Delta y \Delta z \sum_{\substack{x,\,y,\,z \\ \text{such that} \\ \phi(x,y,z) \geq 0.5}} 1 \tag{3.21}$$

Moment of Inertia Ratio

The inertia tensor of an object depends on its mass distribution. Applying this principle to the tumor, we can compare the moment of inertia of a sphere with the same volume and mass. The ratio between the moment of inertia of the tumor and the moment of inertia of the sphere is a representation of how close to a sphere the tumor shape is.

$$R_{MI} = \frac{I_{tumor}}{I_{sphere}} \tag{3.22}$$

The moment of inertia is related with each principal direction of the inertia tensor. Meaning that a 3D object has 3 moments of inertia, the eigenvalues of the inertia tensor. By definition, the inertia tensor is calculated as:

$$I_{ij} \stackrel{\text{def}}{=} \sum_{p=1}^{N} m_p \left(\|\vec{r_p}\|^2 \, \delta_{ij} - x_i^{(p)} x_j^{(p)} \right) \tag{3.23}$$

where δ_{ij} is the Kronecker Delta and m_p and $\vec{r_p} = x_1^{(p)}\hat{\imath} + x_2^{(p)}\hat{\jmath} + x_3^{(p)}\hat{k}$ are the mass and the position vector of point p, respectively. The origin of the referential used to do the calculations was the center of mass of the tumor. Giving an arbitrary density to the tumor, its mass has been considered to be equal to ϕ in every point of the grid.

The sphere moments of inertia are equal and can be calculated from the formula [74]:

$$I_{sphere} = \frac{2}{5} m r^2 = \frac{2}{5} m \left(\sqrt[3]{\frac{3Vol}{4\pi}} \right)^2 \tag{3.24}$$

with the mass and volume equals to those of the tumor.

The approximation from continuous space to the discrete space of the model and the thickness of the interface between tumor and healthy tissue, introduce a small error in the calculation of R_{MI}. This coefficient has a limitation as it fails to represent the correct system once the borders of the simulation grid are reached by the tumor, because of the periodic border conditions.

Chapter 4

Results and Discussion

4.1 Cellular Potts Model

This model possesses an important limitation, as most GP arise from a 3D structure change. This is impossible to be completely described in a 2D simulation. Even so, a 2D model can provide insights regarding the characteristics of the system and the mechanisms that provide duct stability and tumor growth.

4.1.1 Initial Conditions and Rules

The model was built in a 500×300 pixels grid. As all areas and lengths are taken in pixels, and the their target values are inferred from the initial conditions cell type mean values, the pixel side varies slightly between each initial condition. The relative size of cells was approximated from histological images, making each pixel side represents 0.7 to 2 µm, dependent on the initial condition. Figure 4.1 presents the initial conditions used in the simulations and Figure 4.2 compares the initial conditions with histological images. In the latter figure, can be seen that the model preserves the relative size between the different cells' sizes.

The parameters that affect the simulation are the adhesion energy matrix (J), the target area and length, and the respective λ values, the death probability, and the mitosis area. The ranges for these values can be found in Table 4.1 and Table 4.2.

In section 3.1, are described the rules that control the interactions between the cells, presented in Table 4.3. The Sets are ordered by the evolution of the model. This means Set #1 was used in the first stages of development and evolved to Set #3 in the final stages. Set #4 are the rules used to incorporate the *CSC* into the model.

These rules represent properties of certain cell types and conditions, that once met, can

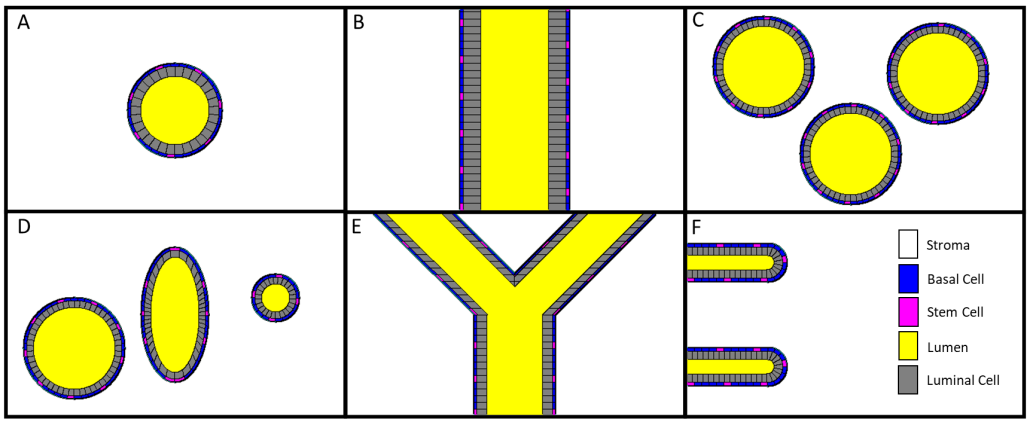

Figure 4.1: Initial conditions used for the CPM simulations.

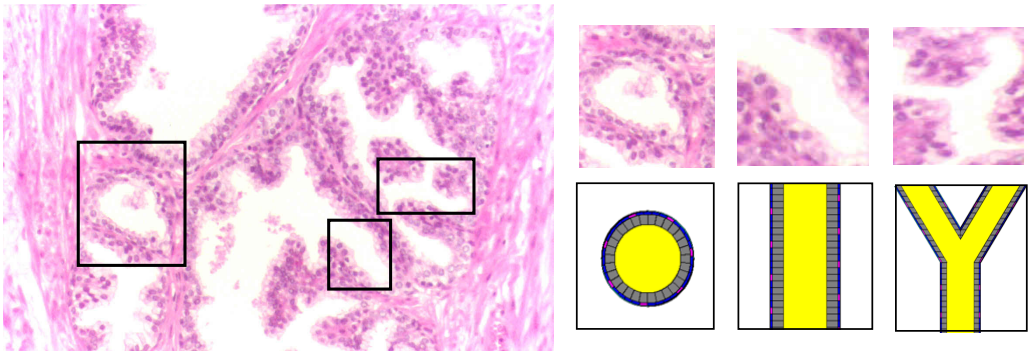

Figure 4.2: Comparison between histologic images and the Initial Conditions. Adapted from [75].

Table 4.1: Range of parameters used. The target areas and lengths are in pixels.

	Stroma	*Stem*	*Basal*	*Luminal*	*Tumor*	*CSC*	*Lumen*
A_{target} [1]	8-12×10^4	35-57	40-57	91-183	91-166	60	2-21×10^3
λ_a	100-10000	100-500	100-500	200-1000	1000	1000	1-10000
L_{target} [1]	-	11-14	11-15	13-21	13-18	11	-
λ_l	0	200-1000	200-1000	200-500	0-1000	500	0
P_{death}	-	-	-	0-0.2	0.1-0.13	-	-
$A_{mitosis}$ [1]	-	-	-	-	91-200	60	-

[1]There are large variations between geometries of the initial condition, and small variations within the same geometry.

Table 4.2: Range of adhesion energy between cell types used.

	ECM	*Stroma*	*Stem*	*Basal*	*Luminal*	*Tumor*	*CSC*	*Lumen*
Stroma	1.8	2.295	1.0-3.0	1.0-3.0	3.0-10.0	3.0-10.0	1.0	3.0-10.0
Stem	1.8	1.0-3.0	1.1-2.4	1.1-2.55	1.2-2.55	1.2-2.55	1.2	2.55-10.0
Basal	1.8	1.0-3.0	1.1-2.55	1.1-2.4	1.0-2.55	1.0-2.55	1.2	2.55-3.0
Luminal	1.8	3.0-10.0	1.2-2.55	1.0-2.55	2.295-2.4	2.295-2.4	2.4	2.55
Tumor	1.8	3.0-10.0	1.2-2.55	1.0-2.55	2.295-2.4	2.295-3.0	1.2	2.55
CSC	1.8	1.0	1.2	1.2	2.4	1.2	10.0	10.0
Lumen	1.8	3.0-10.0	2.55-10.0	2.55-3.0	2.55	2.55	10.0	2.295-3.0

Note: The larger the energy, the weaker the adhesion between cells.

change the properties of individual cells, or activate mitosis and/or differentiation. The following list gives an overview of each rule function in the model.

Rule 1 - Controls the differentiation of *Basal* cells into *Luminal* cells.

Rule 2 - Maintains the type of the epithelium as a single luminal layer (pseudo-stratified).

Rule 3 - Controls the cellular death.

Rule 4 - Controls the homeostatic mitotic behavior of Stem cells.

Rule 5 - Controls the mitotic behavior of *Tumor* cells.

Rule 6 - Controls *Stem* cells movements.

Rule 7 - Controls the adaptive target Area.

Rule 8 - Controls the *ECM* behavior.

Rule 9 - Controls *Lumen* behavior.

Rule 10 - Controls mitosis of polarized cells.

Rule 11 - Maintains the basal layer.

Rule 12 - Controls the *Stem* cells differentiation.

Rule 13 - Controls the mitotic behavior of *CSC*.

Rule 14 - Controls the differentiation of *CSC*.

Table 4.3: The four sets of rules used in the CPM.

Rules	#1	#2	#3	#4
1	If a *Basal* touches the *Lumen*, it turns to a *Luminal*	If a *Basal* touches the *Lumen* or loses contact with the *Stroma*, it turns to a *Luminal*.		
2	If a *Luminal* touches the *Stroma*, it will turn to a *Basal*.	–	If a *Luminal* or *Tumor* is only in contact with *Luminal* or *Tumor*, it will create a *Lumen*.	
3	*Luminal* and *Tumor* have a chance of dying randomly.			
4	When a *Luminal* dies, a *Stem* suffers mitosis.	*Stem* suffers mitosis when a *Basal* cell turns to *Luminal*.	When a *Basal* turns to *Luminal*, the closer *Stem* suffers mitosis.	
5	Above a certain area, *Tumor* will divide; below this area there is a chance of mitosis proportional to time of proliferation.			
6	*Stem* can not move away from stroma.			
7	Target area of *Tumor* varies with time of proliferation.		Target area of *Tumor* and *Lumen* varies with time of proliferation.	
8	–	Any state that reduces the empty space happens, independently of ΔH.		
9	–		*Lumens* that touch merge together.	
10	–		Mitosis divides the cell maintaining the polarization.	
11	–		If a *Tumor* divides maintaining polarization, then the closer *Stem* suffers mitosis.	
12	–		If a *Stem* loses contact with *Stroma*, it turns to *Basal*.	
13	–			*CSC* suffers mitosis after some time, if it has above a certain area.
14	–			*CSC* children will be one *CSC* and one of *Basal*, *Stem* or *CSC* (probabilities can be adjusted).

Some of these rules are directly related to the user-defined parameters. These rules are present here because there is a rational intention in the alteration of those parameters. The reasoning for the evolution of rules between each Rule Set are presented in the next sections.

4.1.2 Rule Set #1

When the CPM was created, it was given some rules to maintain the homeostasis seen *in vivo*.

Rule 1 and *Rule 2* were meant to maintain the differentiation in the basal and luminal layers of the epithelium. The former by forcing *Basal* cells in contact with the *Lumen* to be *Luminal* cells, and the latter by forcing *Luminal* cells in contact with the *Stroma*to be *Basal* cells, in order to act like an intermediate cell, a type of prostate cells not modeled with affinity to be in contact with the *Lumen* and the *Stroma*.

Rule 3 and *Rule 4* imposes the cellular renovation seen in epithelia. Cells of the luminal layer will die randomly and *Stem* cells will proliferate to maintain homeostasis.

Rule 5 defines the *Tumor* cells proliferation characteristics, a maximum growth and a time dependency.

Rule 6 prevents normal *Stem* cells to move from the *Stroma*. A high expression of integrin $\alpha 2\beta 1$ fixates stem cells to the basal membrane [28], that is modeled by the stroma. If a *Stem* cell loses contact with the *Stroma*, then it would create a basal zone with multi-layers.

Rule 7 slows the growth rate of *Tumor* cells. By setting the target area to the value of a mature cell immediately after mitosis, would force the *Tumor* cell to achieve its target area within a few iterations. The *Rule* ensures a steady growth that that takes in account the other model parameters, such as length and adhesion.

The model was tested without *Tumor* cells to verify its stability (Figure 4.3).

This results show that the model would fail to maintain the homeostasis of the system. Cellular death would form spaces without cells (or *Lumen*), the luminal and basal layers would lose their continuity and *Rule 1* and *Rule 2* would conflict with each other due to the lack of two layers.

With this fail to model the proper behavior of the prostate gland, comes the insight to hypothesise that the maintenance of luminal and basal layers is assured by a larger number of mechanisms. This suggests that maintenance of a constant number of cells in the prostate is not only ensured by having the same proliferation rate of *Stem* cells as the death rate of *Luminal* cells, and some higher control must be in place.

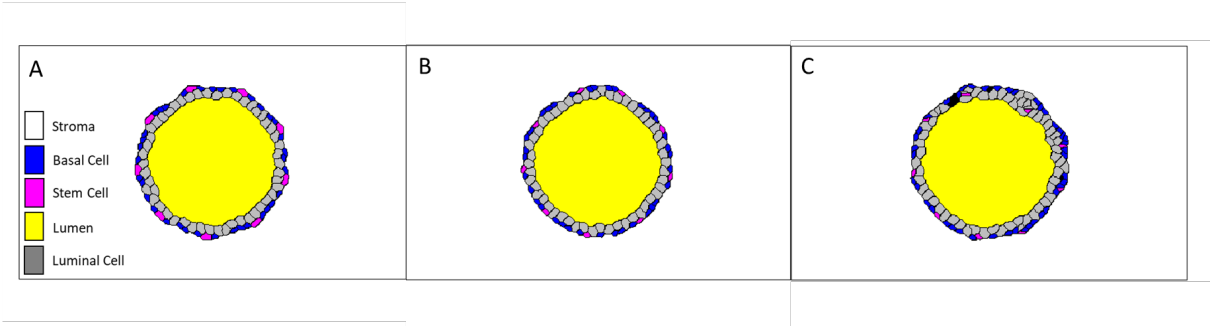

Figure 4.3: Stability test. The images represent the simulation after 1170 time steps. In both simulation A and B, no cellular renovation is present, as the death rate is set to 0. In simulation C the death rate is 0.1‰. The parameter and adhesion energy values can be found in Table A.1 and Table A.2

4.1.3 Rule Set #2

The problems and hypothesis from the first model were tested by adapting the rules as follow:

Rule 1 changes to also allow a momentaneous appearance of more than one layer of *Luminal* cells, an occurrence frequently seen in histologic images of the prostate. This rule also eliminates any possibility to accumulate *Basal* cells. However to compensate this process the adhesion between *Basal* cells and *Stroma* was kept high (low adhesion energy), avoiding its separation. The intermediate cells, treated as *Luminal* cells in the model, can be simultaneously in contact with both lumen and the basal membrane in the prostate. So, besides the addition to *Rule 1*, *Rule 2* was eliminated on the premise that cells follow a one way differentiation process, and that the adjustment of the previous rule ensures the proper differentiation process.

Due to the discontinuity that appeared with the previous set of rules, the proliferation of *Stem* cells was adjusted. When a *Luminal* cell dies, a *Basal* cell must differentiate to occupy its place and a *Stem* cell must proliferate to maintain the number of cells. However, because of small oscillations there can be more *Basal* cells differentiating than the number of *Luminal* cells that died. To compensate for this possibility, maintaining the basal layer, *Rule 4* was adjusted so that *Stem* cells proliferate when a *Basal* cell disappears instead of a *Luminal* cell dying.

Cellular death leaves a space without cells and only *ECM*. This means there is an area that can be occupied, and, in nature, this is a fast process. Therefore, *Rule 8* was implemented to force the empty space to disappear even if energetically unfavorably. This rule was added because the model does not consider all variables that exist, such as pressure, that would force the space to be occupied.

With these four changes to the rules, the stability was tested again (Figure 4.4). For this model, the stability of the system became possible for certain combinations of parameters.

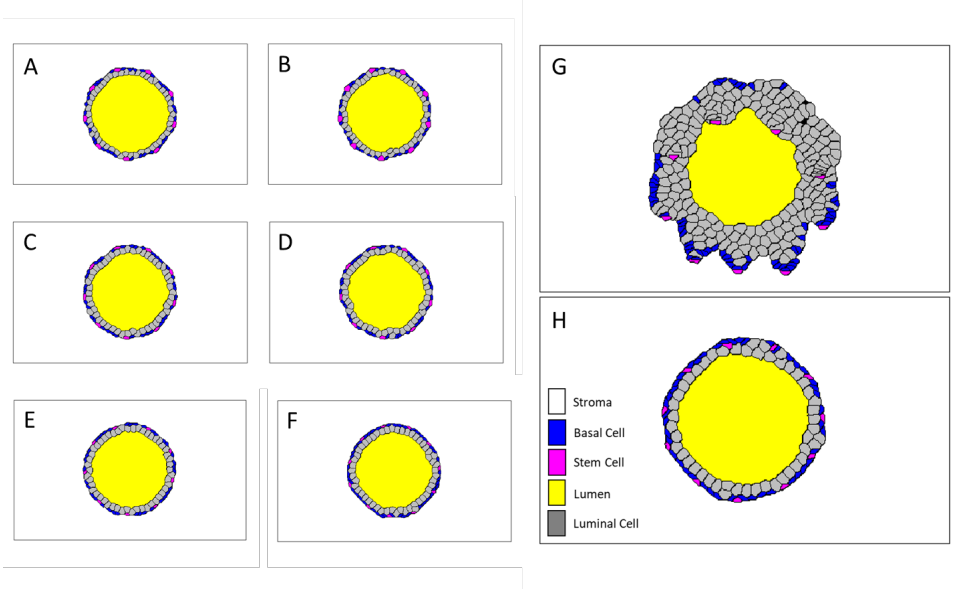

Figure 4.4: Stability tests (Rule Set #2). The images represent systems with different parameters at the 3000$^{\text{th}}$ iteration. The parameters used in the simulations can be found in Tables A.3 to A.7.

One clear result was that a higher cell mortality would cause the *Stem* cells to proliferate faster than the *Basal* cells could migrate around the basal layer to fill the empty spaces. This would result in the accumulation of *Basal* cells that would turn to *Luminal* cells due to *Rule 1* (Figure 4.4-G has the higher probability of *Luminal* cells dying-0.2‰, while Figure 4.4-E has the same parameters without cellular death). This situation shows how the cellular death limits the system. As 1-2 % of the total prostatic cells are renovated daily [18,19], and the limit to the probability of cellular death to maintain homeostasis is around 0.1‰, it can be assumed for the model to have around one hundred MCS per day.

Other variations can be seen when changing the values of λ_a and λ_l for the different cell types. The importance of a high value of these parameters in *Stem*, *Basal* and *Luminal* cells can easily be seen in Simulations A, B, C and D of Figure 4.4, where these cell types shrink below the expected size. The consequence of this effect is the discontinuity of the basal layer, that becomes less evident over the simulations as the λ values for these cell types increase. For the other cell types, the increase in these parameters, offers more resistance to duct deformation, despite being less evident.

Although the model intends to simplify most of the processes in the prostate, its complexity can be seen in the limited combinations of parameters that achieve a homeostatic system, as achieved in Figure 4.4-H.

With this homeostatic system, *Tumor* cells can be included to analyze PCa growth (Figures

4.5 and 4.6). The tumor development in this simulation is fast and creates one structure that

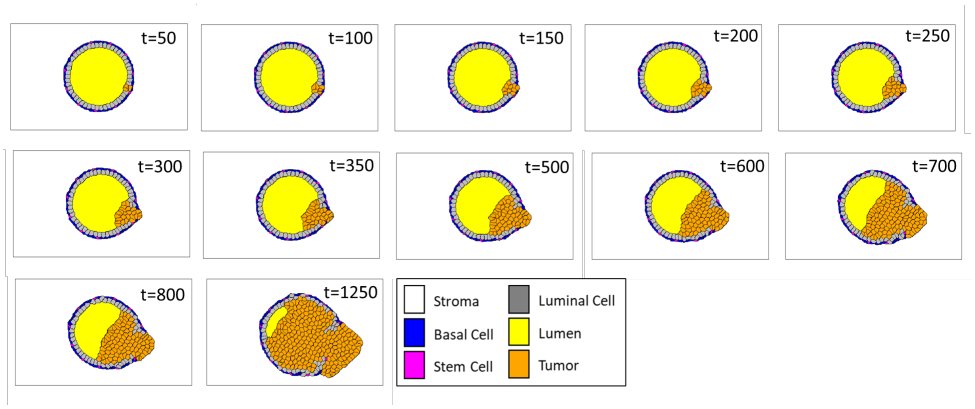

Figure 4.5: Tumor growth in a single duct. The parameters can be found in Tables A.8 and A.9.

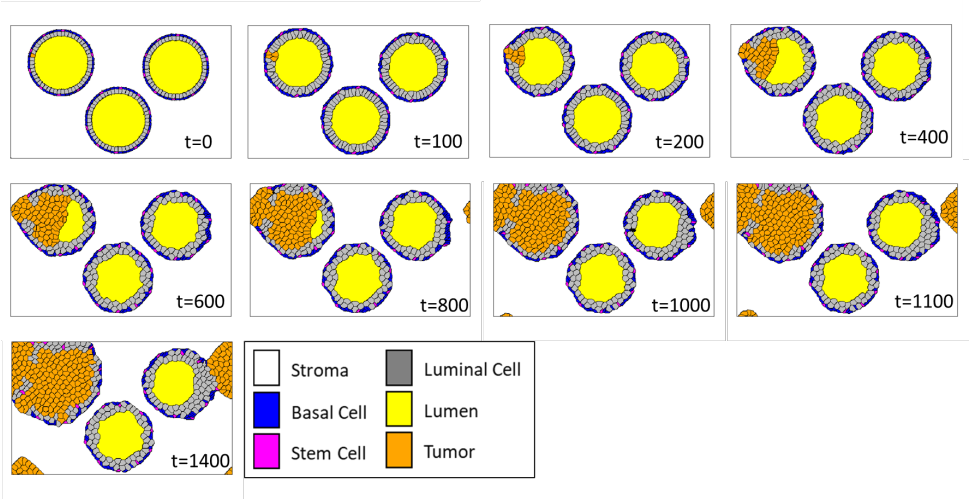

Figure 4.6: Tumor growth in multiple ducts. The parameters can be found in Tables A.8 and A.9.

is characteristic of high grade PCa, the Solid pattern. Even in the simulation of Figure 4.6, the tumor mass grows independently of the ducts original geometry, creating a Solid pattern. This shows that PCa growth can not be modeled by a simple proliferation of *Tumor* cells. Although the infiltrative behavior can be adjusted with the stroma properties, namely the adhesion energy between *Tumor* and *Stroma*, or the combination of λ_A and A_{target} of the *Stroma* type.

The desired observation would be to get the formation of the different GP for different combinations of parameters and geometries (Figures 4.5, 4.6 and 4.7). However, the simulations only created solid patterns with the shape of the tumor mass changing with the different geometries. Therefore, one would expect the appearance of the clinically irrelevant patterns (GP1 and 2) where the shape of the glands is maintained but the distances between them increases. It is not clear in the community the reason behind this process. Several possible mechanisms were

explored using the model. One was that the *Tumor* cells in the ducts intersections may cause the spacing between the ducts. Other was that tumor mass forces the stroma to move to provide space, increasing the distance between glands.

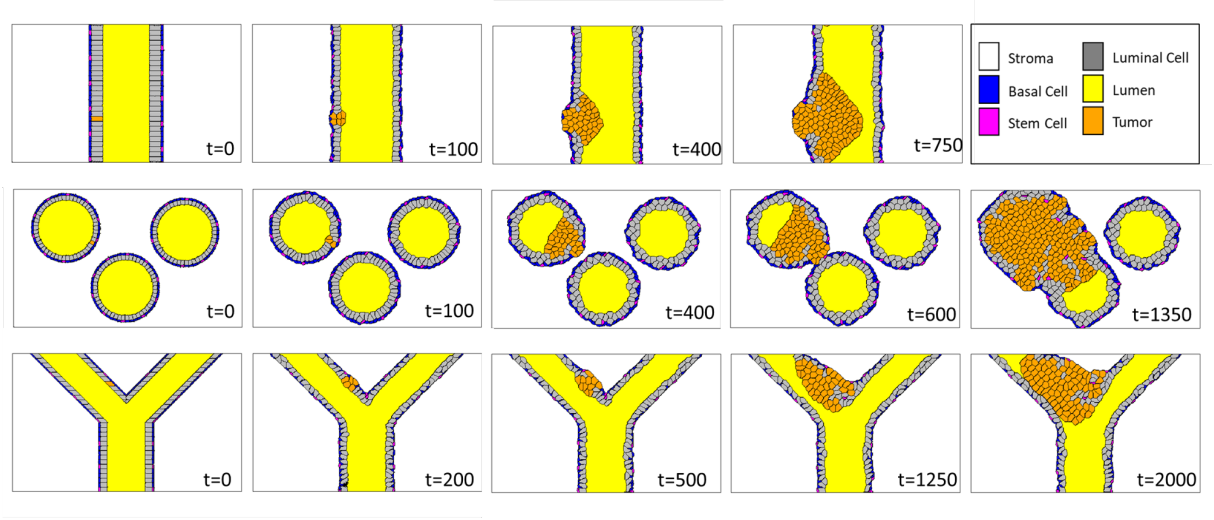

Figure 4.7: Tumor growth over different duct geometries. The parameters can be found in Tables A.10 and A.11.

The attempts to force the separation of glands always resulted in the formation of a Solid pattern. Once the *Stroma* resistance to infiltration was increased, the tumor would occupy the gland. If infiltration was possible, smaller ducts at a larger distance could appear. However, the *Tumor* cells would still form a solid GP5.

Another hypothesis, based on the cellular properties, could be tested. Tumors maintain some characteristics of the cell types from which they are originated, which allows to determine its histologic origin (95% of PCas are luminal-like adenocarcinomas) [24,26]. With this information, the *Tumor* cells can be adjusted to maintain some characteristics of *Luminal* cells. This led to a further adjustment to the model.

4.1.4 Rule Set #3

Two properties were included in the *Tumor* cells. One was the polarization that can be seen in epithelium cells. Most epithelium cells, namely luminal cells, have a different membrane composition on the luminal and basal sides, as they secrete to the lumen instead of secreting to the tissue [76]. The other property added was derived from the same motivation, giving *Tumor* and *Luminal* cells the capacity to form new *Lumens*. If these cells have polarization, and a membrane domain that does not adhere to other cells, then a space (a *Lumen*) is formed.

A lumen surrounded by secretory cells is a gland, that can originate from a larger one. The

new smaller glands can be close to others and if they separate, the distance between glands increases forming both GP1 and 2, respectively.

Rule 2 is meant to control the luminal layer and has been removed in the previous set of rules. To add the *Lumen* formation capacity to the model, the *Rule* will now create new *Lumen*s where a high concentration of *Luminal* and *Tumor* cells are present.
Rule 4 was adapted to facilitate the appearance of basal layer around the depleted zones to maintain the homeostatic behavior where the tumor affects the gland. As most *Basal* cells turn to *Luminal* when another *Luminal* cell dies, this *Rule* is an application of a paracrine signalling due to cellular death to stimulate local *Stem* cell proliferation.
Rule 7 evolves to include the *Lumen* type. However, the relation between time of proliferation with *Tumor* and *Lumen* target area is different. The former increases with time of proliferation, while the latter initially increases to prevent the collapse of the recently formed *Lumen*, and is removed ($A_{target} = A$) after some time, to give the new *Lumen* the same behavior as in the previous models.
Rule 9 prevents the physical impossibility of two *Lumen*s being in contact. Even if computationally possible, *Lumen-Lumen* interface would create an instability in the model as it allows the migration of other cells in the interface. *Rule 10* forces the *Tumor* and *Stem* cells to divide while maintaining the basal and luminal layers of the epithelium. Mitosis does not divide cells along a random axis. The mitotic axis is defined according to the internal cellular polarization [77]. Although the effect on *Stem* cells is almost negligible in the model, the effect on *Tumor* proliferation is relevant. Maintaining the polarization on mitosis means that the axis of division is perpendicular to the orientation of the layers. Therefore it prevents to a certain extent the formation of one single mass of tumor cells. However, if a *Tumor* cell is not in contact with *Lumen* and a cell of the basal layer, it will be considered to have no polarization and divide along the longer dimension.
Rule 11 makes the *Stem* cells proliferate to maintain the basal layer when the *Tumor* cells proliferate without the formation of tumor masses. This prevents tumor infiltration of the *Stroma*.
Rule 12, like *Rule 6*, prevents the *Stem* type from exhibiting the behavior characteristic of *CSC*.

This model shows the formation of a Cribiform pattern (Figure 4.8), that is characteristic of GP4. However, as more *Lumen* appear, more the appearance of GP1 is revealed. The longer a new *Lumen* exists, the more circular it became as the *Tumor* cells surround it and form a new gland. Because the simulation models the beginning of PCa, any patient at this stage would still be considered healthy, therefore no clinical data exists.

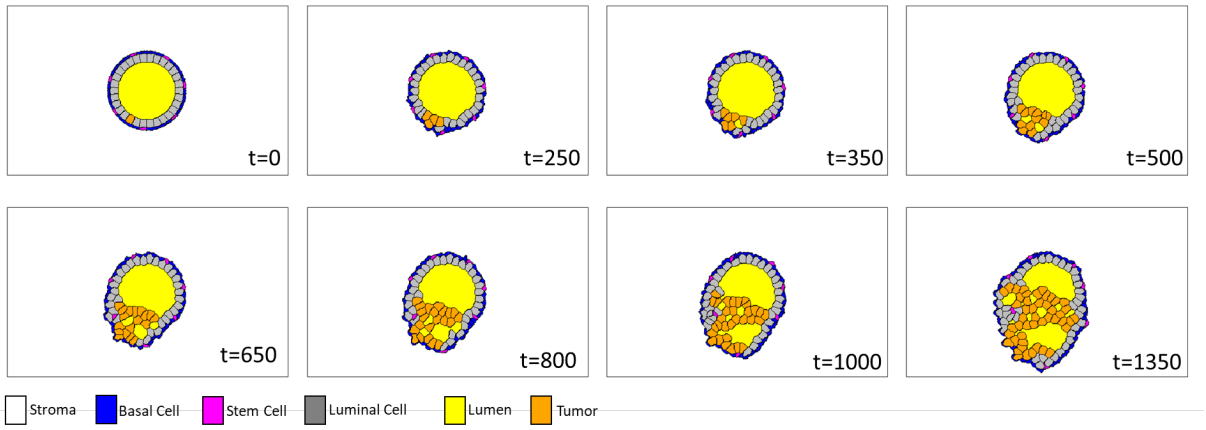

Figure 4.8: Simulation with cribriform GP. The parameters used in the simulation can be found in Tables A.12 and A.13.

Considering this, the model may allow to propose that if *Tumor* cells maintain the innate capability to form the epithelium structures of the prostate, the tubeloalveolar network, then new well defined prostate glands (GP1) would be seen in a tissue slice. Moreover, if these glands permitted stroma to appear between them to form seperate ducts, they would force an increase of the inter-gland distance (GP2).

4.1.5 Rule Set #4

To this point, the direction taken in the model is unable to describe the formation of a higher grade GP. These patterns derive from a change in number and shape of the prostate ducts [42](see section 2.2.3). Because of the controversial origin of PCa (subsection 2.2.1), a new model was created to incorporate a tumor where the cells have different proliferation rates. To achieve this result, the Cancer Stem Cell (CSC) type was defined with the properties defined in *Rule 13* and *Rule 14*.

Rule 13 defines *CSC* proliferative activity as the *Tumor* type. Above a certain area the cell will be able to divide originating two.

Rule 14 defines the distint characteristic of *CSC* type, one of the daughter cells may lose its proliferative capacity and differentiate.

This new cell type correspond to a tumor cell capable of originating new epithelial tissue. The goal for this approach is to achieve, in a longitudinal cut, the formation of new interconnections and shape changes on the prostate network, characteristic of GP3, 4 and 5.

In this model the *Basal* type cells (that differentiates to *Luminal*) generated from the *CSC* cells, must be considered tumorous cells with the corresponding degree of differentiation and

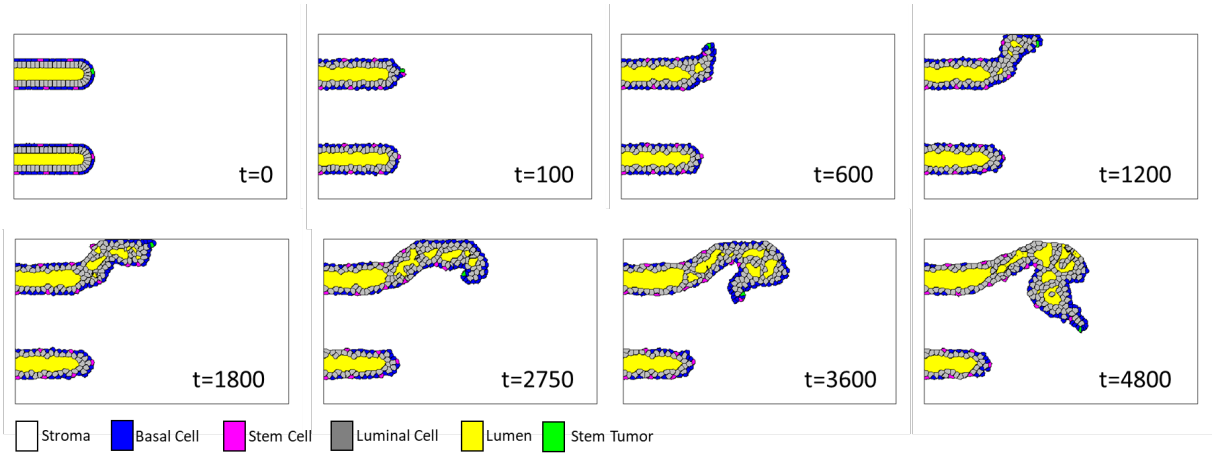

Figure 4.9: Simulation with *CSC*. The parameters can be found in Tables A.15 and A.15.

without proliferative capacity. *Tumor* type cells can originate from *CSC* cells, and would behave as in the previous models. As can be seen in Figure 4.9 when comparing to the previous simulations, the *CSC* type creates a lesion that propagates further than the lesions caused by the *Tumor* type. This could cause the appearance of different types of tumors patterns in different zones of the prostate, thus providing an explanation for the different GP found in a single biopsy.

4.2 Phase-Field Model

4.2.1 Initial Conditions

A simulation box of $1000 \times 1000 \times 1000$ µm was used with a spacing between points of 5 or 10 µm.

The prostate ductal network was implemented, by defining the order parameter θ, as the branched-tree geometry, seen in Figure 4.10. This geometry allows to observe the interaction between ducts of different diameters as the tumor grows. The tumor started as a sphere with 50 µm of diameter.

4.2.2 Ducts Implementation

Firstly, the prostate network was implemented in the phase-field model. Equation (4.1) to (4.5) represent the different hypotheses tested to adapt Equation (3.14).

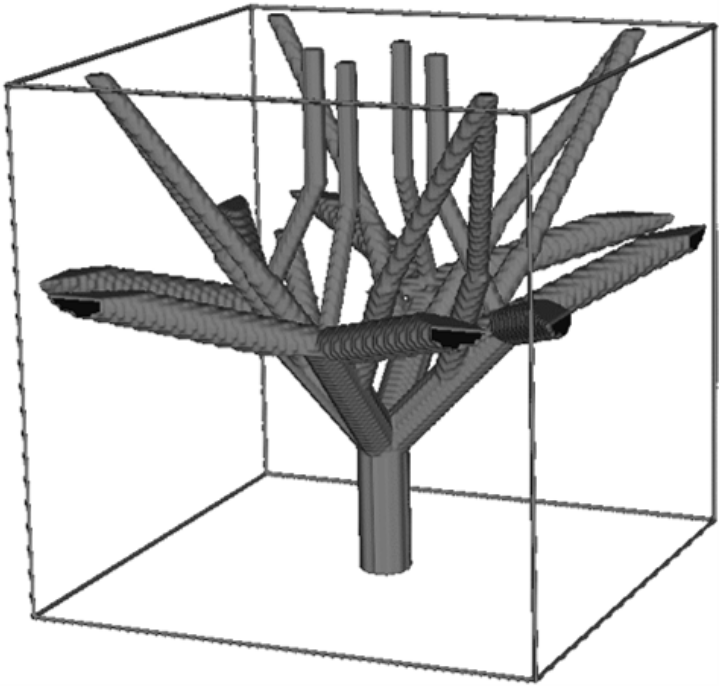

Figure 4.10: Ducts shape inside the simulation box. This image shows the places where $\theta = 0$ (ducts) while the tissue ($\theta = 1$) is transparent.

As a Diffusion limiter

As at the early stages the tumor is mostly maintained inside the ducts, the diffusion of tumor was limited to their interior.

$$\frac{\partial \phi}{\partial t} = (1 - \theta\phi) \times \left[\lambda \nabla^2 \phi + \frac{64}{\tau}(1 - \phi)\left(\phi - \frac{1}{2}\right)\right] + \chi\sigma\phi - A\phi \tag{4.1}$$

$(1 - \theta\phi)$ varies between 0 and 1, being 0 where tumor exists and ducts do not ($\phi = 1$,$\theta = 1$), and 1 otherwise. Multiplying $(1 - \theta\phi)$ by the terms responsible for the diffusion of the tumor, only allows the diffusion of tumor in the ducts ($\phi = 1$, $\theta = 0$).

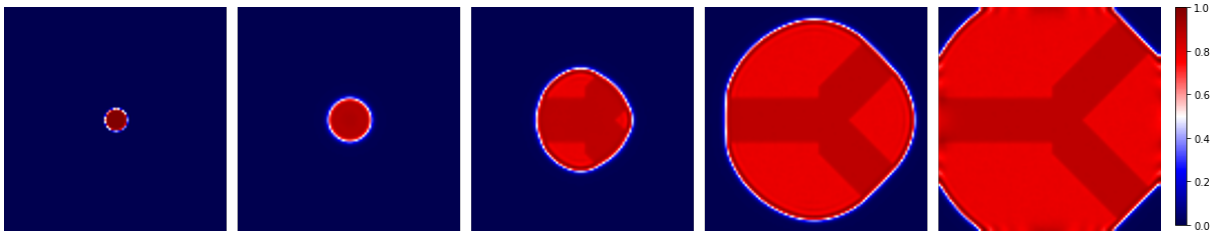

Figure 4.11: Simulation of Equation (4.1). The images correspond to the middle slice of the simulation box. In this simulation the ductal network is simplified to one bifurcation.

However, as proliferation exists where tumor and nutrient exists, it creates a region in the tissue where tumor can appear, and, at the interface between tumor and no tumor ($\phi \approx 0.5$),

diffusion is still possible in the tissue ($\theta = 1$), albeit slower. This results in the outcome of Figure 4.11. In a phase-field model there should be one zone with $\phi = 1$, one zone with $\phi = 0$ and a thin interface between them. This model does not satisfy the minimum conditions of a phase-field model.

As a Diffusion and Proliferation limiter

Based on the same principle than before we can limit the proliferation of tumor to the ducts,

$$\frac{\partial \phi}{\partial t} = (1 - \theta\phi) \times \left[\lambda \nabla^2 \phi + \frac{64}{\tau}(1-\phi)\left(\phi - \frac{1}{2}\right) + \chi\sigma\phi\right] - A\phi \tag{4.2}$$

This equation limits the diffusion and the proliferation by the term $(1 - \theta\phi)$. This prevents the tumor to proliferate or diffuse in the tissue, forcing it inside the ducts.

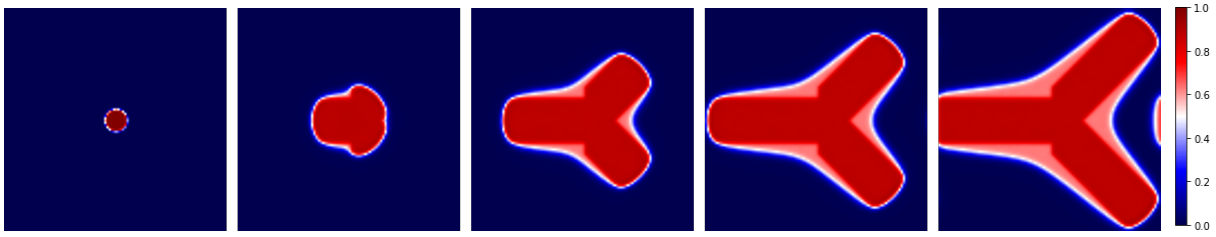

Figure 4.12: Simulation of Equation (4.2). The images correspond to the middle slice of the simulation box. In this simulation the ductal network is simplified to one bifurcation.

However, as seen in Figure 4.12, the possibility of diffusion in the interface discussed previously still allows for tissue invasion starting at the ducts bifurcations.

As an Energy term

The second term of Equation (3.14) represents the derivative of an energy function that forces the separation of phases (tumor and healthy, 0 and 1). In the same way, the ducts can be introduced in an energy function that reduces the system energy inside the ducts.

$$G(\phi) = \frac{\theta^2(2\theta - 3)\phi^2(2\phi - 3)}{2} \tag{4.3}$$

This function is 0 when $\theta = 0$ and has a minimum for $\phi = 0$ when $\theta = 1$. This means that, when the tumor is outside of the ducts, it will have more energy. However, if the tumor is inside of the ducts, the contribution from $G(\phi)$ will be null. Adding the new energy term to Equation (3.14), becomes:

$$\frac{\partial \phi}{\partial t} = \lambda \nabla^2 \phi - \frac{1}{\tau}\frac{dF(\phi)}{d\phi} + \chi\sigma\phi - A\phi - \mu\frac{dG(\phi)}{d\phi} \tag{4.4}$$

where μ controls the influence of the ducts. The larger the μ, the more contained the tumor is inside the ducts. Expanding the terms:

$$\frac{\partial \phi}{\partial t} = \lambda \nabla^2 \phi + \frac{64}{\tau} (1 - \phi) \left(\phi - \frac{1}{2} \right) + \chi \sigma \phi - A\phi - 3\mu\theta^2 (2\theta - 3) \phi (\phi - 1) \tag{4.5}$$

This change makes the tumor growth inside the ducts more favorable while allowing the infiltration of the tumor in the tissue with some resistance.

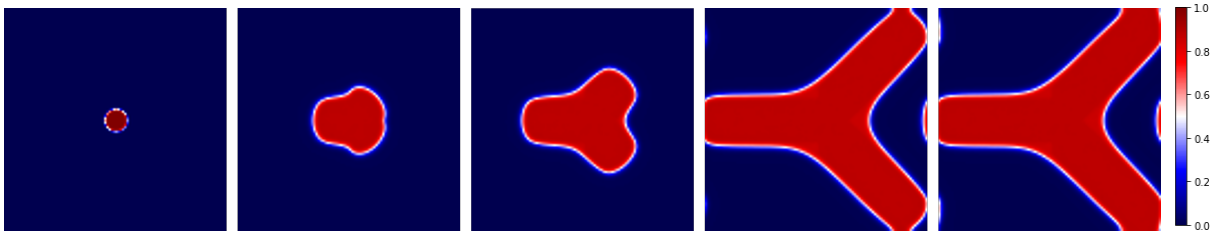

Figure 4.13: Simulation of Equation (4.5). The images correspond to the middle slice of the simulation box. In this simulation the ductal network is simplified to one bifurcation.

In Figure 4.13, it can be seen that the tumor-healthy tissue interface is not affected, while the tumor growth is contained within the ducts.

4.2.3 Simulations

Testing the model, it is possible to see the influence that each parameter has in the tumor evolution and to analyze the qualitative similarity with real cases.

The model is defined by Equation (3.16) and Equation (4.4):

$$\frac{\partial \sigma}{\partial t} = \epsilon \nabla^2 \sigma + s - \delta \phi - \gamma \sigma$$

$$\frac{\partial \phi}{\partial t} = \lambda \nabla^2 \phi - \frac{1}{\tau} \frac{dF(\phi)}{d\phi} + \chi \sigma \phi - A\phi - \mu \frac{dG(\phi)}{d\phi}$$

With the values of $\lambda = 50\ \mu\mathrm{m\,s^{-1}}$, $\tau = 3.65$ d, $A = 1.6438\ \mathrm{d^{-1}}$, $\epsilon = 50 \times \lambda$, $s = 2.75 \pm 0.25\ \mathrm{g\,L^{-1}}$, $\delta = 2.76\ \mathrm{g\,L^{-1}\,d^{-1}}$ and $\gamma = 2.75\ \mathrm{d^{-1}}$, the effect of the variation in proliferation (χ) and the influence of the ducts (μ) were analyzed.

Proliferation

As expected for a tumor, the larger the proliferation the faster the tumor grows. Figure 4.14 shows the influence of χ in the growth rate of the tumor when μ is constant, with value 0.2. On the first row of Figure 4.14, a tumor can be seen reducing its volume very slowly. This marks

the minimum value of proliferation for the combination of parameters used. For smaller values of proliferation ($\chi \leq 1.05$) the tumor disappears completely, in less than 60 days (Figure 4.15).

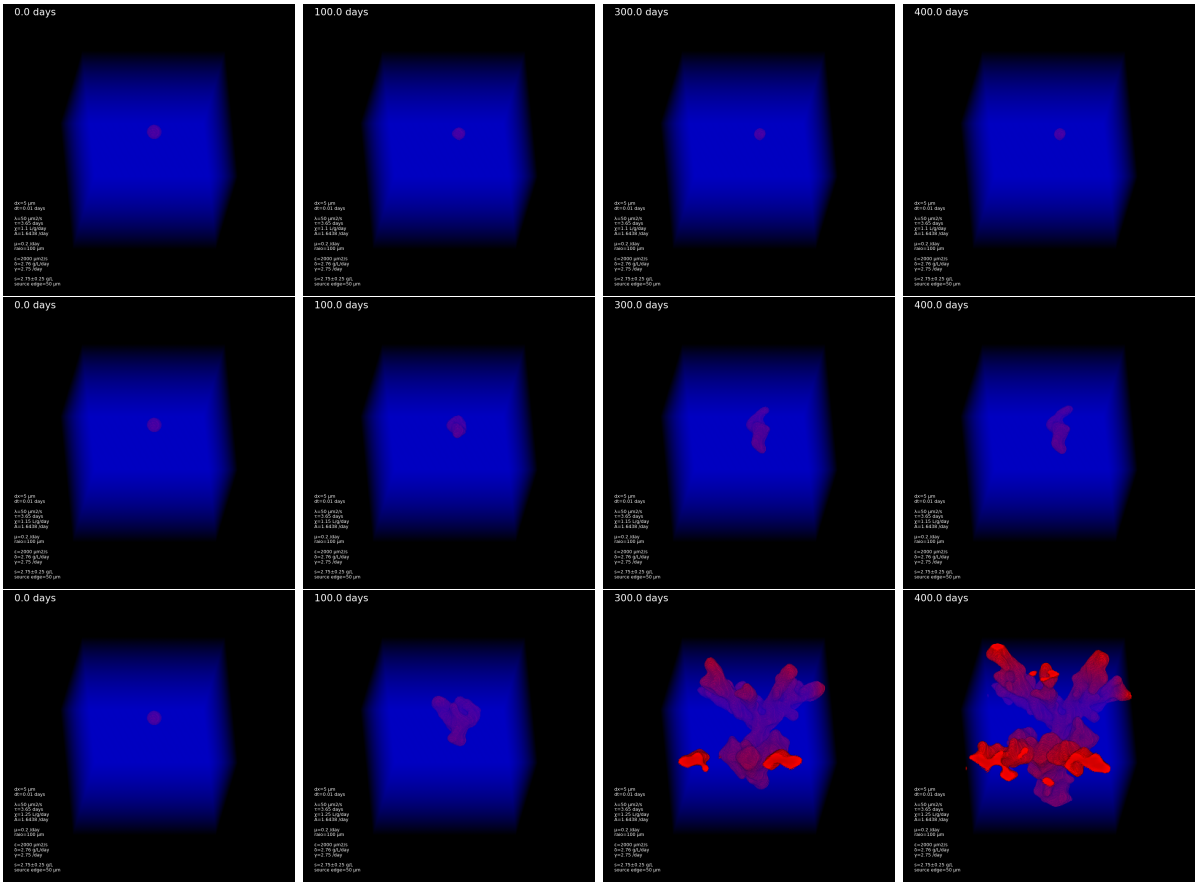

Figure 4.14: Effect of χ in the model. From left to right, it can be seen the progression of the simulation. From top to down, it can be seen the increase in the proliferation constant (χ=1.10,1.15,1.25), and its effect in tumor growth rate. The initial tumor is contained inside the ducts in all simulations.

These results show that, for the model, there is a minimum rate of proliferation required for the tumor to thrive or even survive. Patients have an immune response to PCa [78], therefore it is expected that a lower proliferation rate will result in tumor regression.

Ductal network influence

The prostate micro-morphology influences the path for tumor growth. However, it has very little contribution for the total volume growth rate, as seen in Figure 4.16. For a certain proliferation rate, the effects of the resistance to infiltration are only visible in the tumor shape, meaning a minimum variation in tumor volume. However, the longer the tumor grows the more visible is the influence of the ducts.

Decreasing μ results in less energy being required for the tumor to leave and deform the

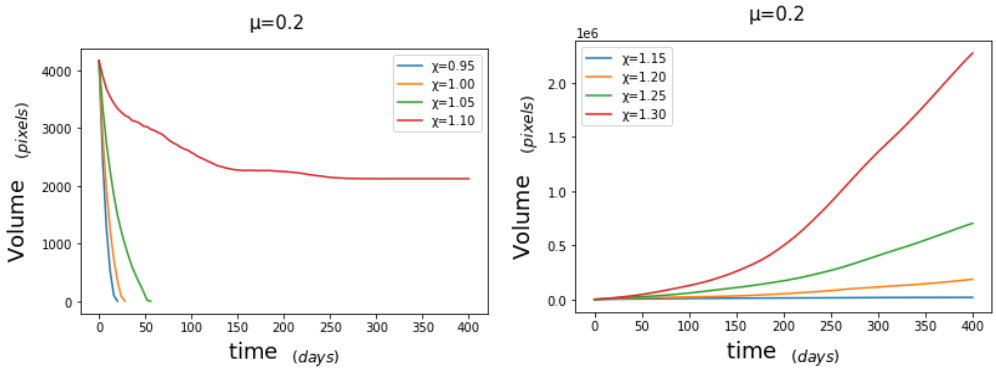

Figure 4.15: Tumor volume as a function of time for different values of χ. The tumor can only proliferate if χ is larger than 1.15. The data is split in two plots with different vertical scales for easier visualization. The volume of the tumor from the simulations in Figure 4.14 are included in these plots.

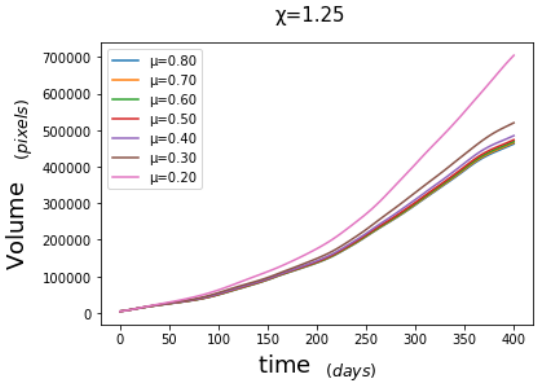

Figure 4.16: Volume of the tumor in function of time, for different values of ducts resistance.

ducts. In PCa, the ducts are deformed changing size and shape, originating the GPs [10, 42]. Therefore, this is seen for smaller values of μ.

In Figure 4.17, a slice of the simulation box can be seen as a H&E slice would be. When the tumor growth is facilitated inside the ducts, without much resistance (low μ), new non-spherical tumorous glands can be seen appearing as expected from a GP2 and GP3. If the ducts resistance is too high, then the tumor would stay restrained to the original ducts, without creating the structures of the GPs. This means that the model must use $\mu \leq 0.2$.

Overall

With the parameters defined, the simulation can be compared to PCa patients histologic results. Figure 4.18 shows the simulation box (ϕ) sliced at different heights overlaid with the original ducts (θ).

It can be seen the continuous change from multiple glands to an increase in interconnections

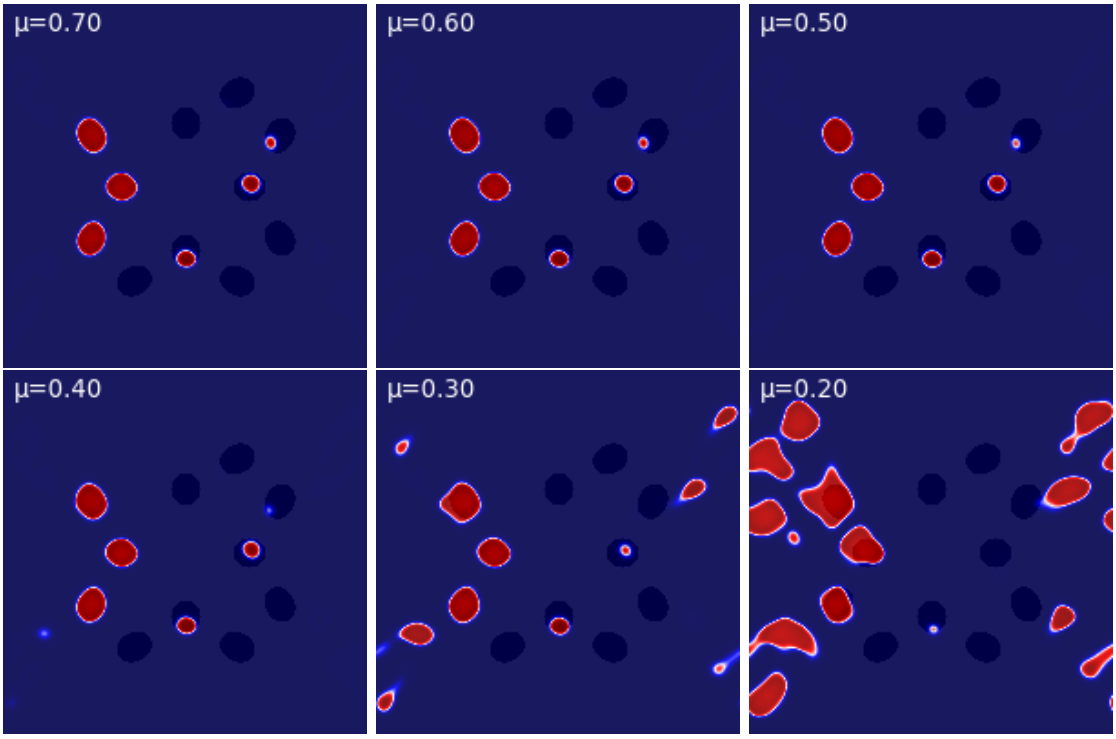

Figure 4.17: 2D slice of the simulation. The slices were captured at the 400$^{\text{th}}$ day, with $\chi = 1.25$. The tumor (red) is overlaid with the original ducts (dark blue) for better analysis.

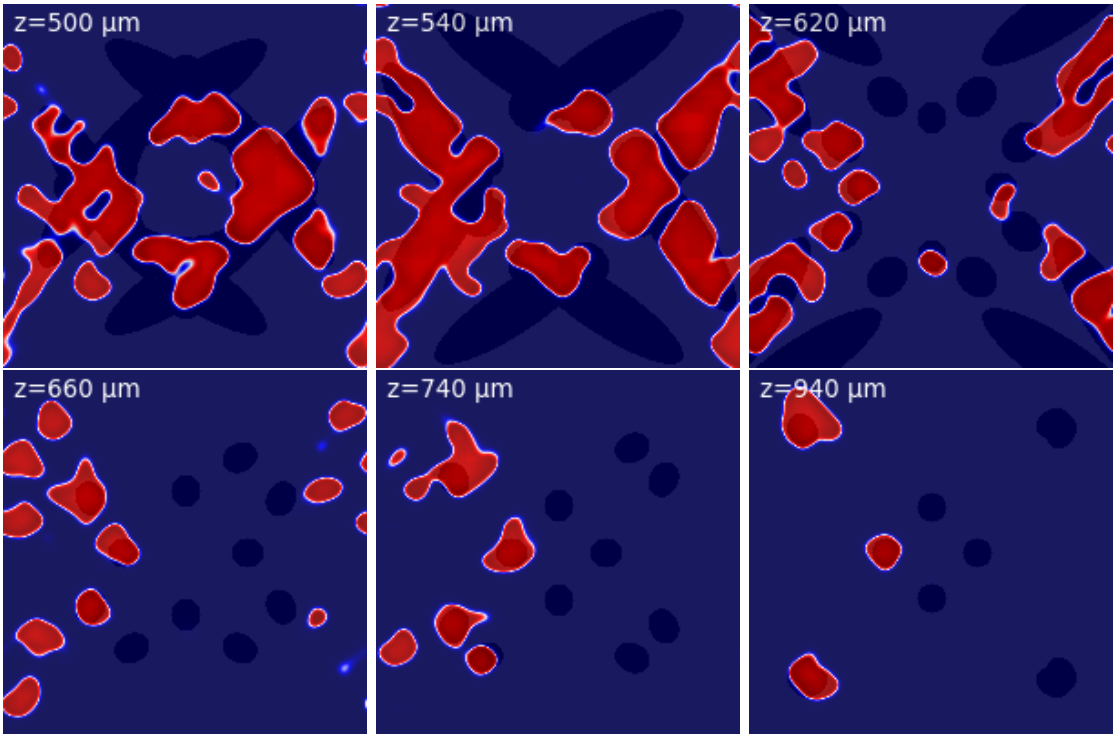

Figure 4.18: Slices at different heights. This represent the 400$^{\text{th}}$ day of simulation with $\chi = 1.25$ and $\mu = 0.2$. The tumor (red) is overlaid with the original ducts (dark blue) for better analysis.

as described in the work from Leenders *et al* [42] when they observed the GP3 continuously with Poorly Formed GP4. In the simulation of Figure 4.18, the GP3 can be seen at z=660 µm and GP4 at z=500 µm. The simulation suggests this structure is formed as the tumor deforms the ducts and grows in that specific direction, creating a new duct or alveoli in the space previously occupied by the stroma. The tumor growth creating this structures can be seen in Figure 4.19

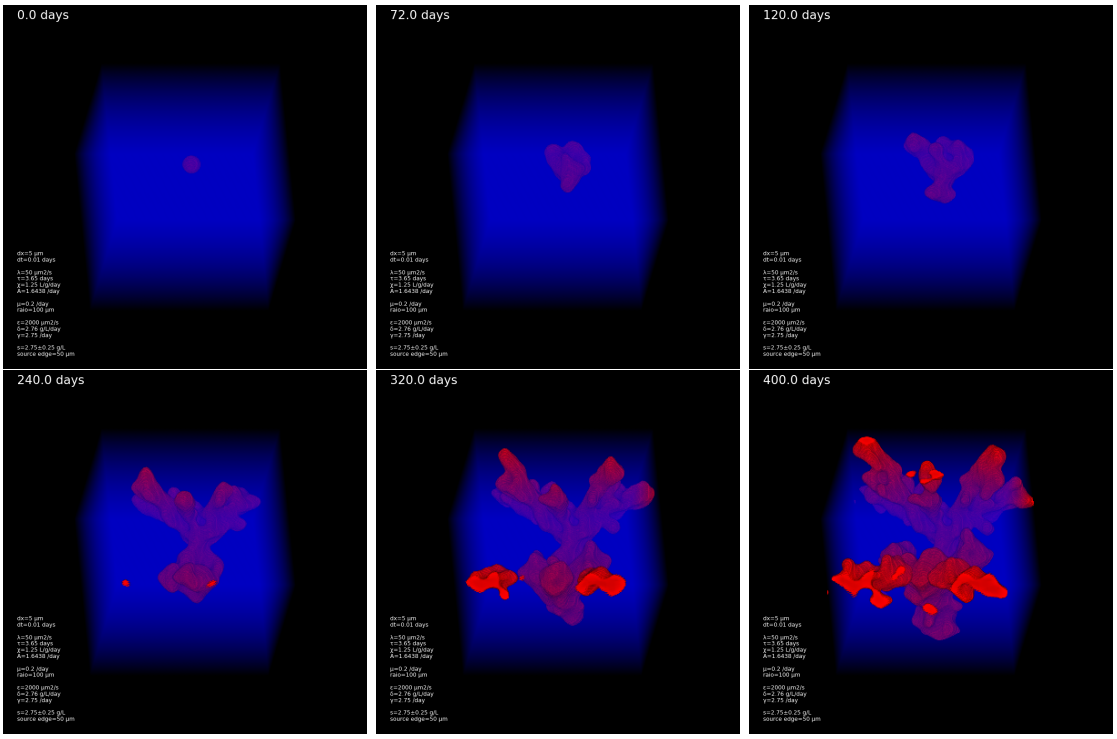

Figure 4.19: Simulation of tumor growth over 400 days with $\chi = 1.25$ and $\mu = 0.2$.

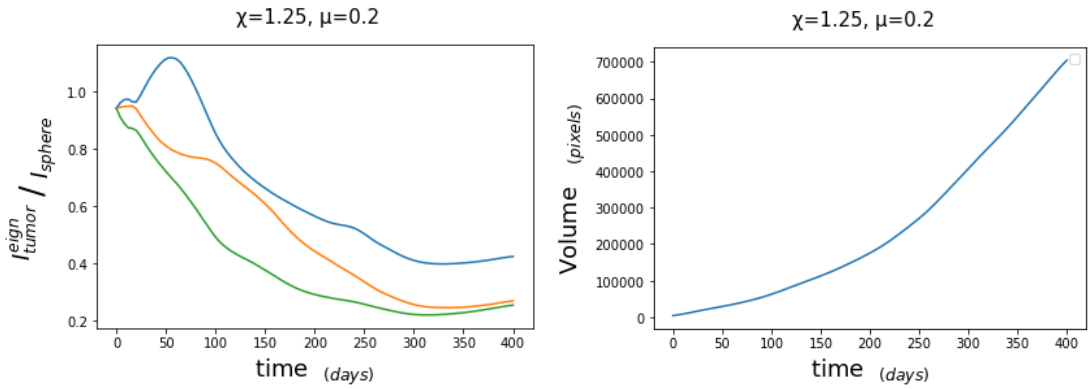

Figure 4.20: Moment of Inertia Ratio and Volume of the tumor in Figure 4.19. The 3 curves in the left plot correspond to each of the eigenvalues of the inertia tensor.

The Moment of Inertia ratio decreases steadily over the simulation, as expected from the tumor to avoid starvation, having a non-spherical growth, while the total volume of tumor

grows exponentially (Figure 4.20). In this model the ducts are rigid and the infiltration over the stroma/tissue is considered as deformation of the ducts, because this phenomenon is more common, and usually preliminary to infiltration of the stroma.

4.2.4 Ducts Deformation

So far, the model has considered the ducts as a fixed variable that provide a path for the tumor to growth. However, the tumor presence affects the ducts, deforming them. If the deformation of the ducts and the tumor are treated separately, although dependent, it is possible to evaluate the tumor infiltration and have more information about the structures created by the tumor.

Variation in the ducts shape can be included by transforming the tissue/ducts (θ) in a phase-field affected by the tumor (ϕ), with the equation:

$$\frac{\partial \theta}{\partial t} = -\omega\phi \quad , \qquad 0 \leq \theta \leq 1 \tag{4.6}$$

where ω is the rate of disappearance of tissue in the presence of tumor. The disappearance of tissue is used to describe the phenomena that cause the volume of the tissue to decrease (volume of the ducts to increase). Mechanical strength (pressure due to the tumor) and collagen degradation (ECM degradation) [79] are examples of such phenomena.

Preliminary Results

It is possible for ϕ to be outside the interval $[0, 1]$ by a small margin, and, for large values of χ or A, may cause the model to diverge. To further improve the model, when introducing variation in the ducts with Equation (4.6), the stability of the tumor dynamics was improved.

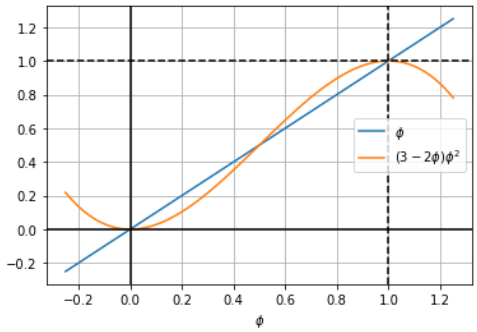

Figure 4.21: Demonstration of the changes in proliferation and apoptosis from Equation (4.5) to Equation (4.7)

Replacing ϕ for $(3-2\phi)\phi^2$ in the terms associated with proliferation ($\chi\phi$) and apoptosis ($A\phi$) of the tumor in Equation (4.5), provides a similar behavior when $\phi \in [0,1]$ and prevents the escalating effect outside the interval (Figure 4.21). The dynamics of ϕ became:

$$\frac{\partial \phi}{\partial t} = \lambda \nabla^2 \phi + \frac{64}{\tau}(1-\phi)\left(\phi - \frac{1}{2}\right) + (\chi\sigma - A)(3-2\phi)\phi^2 - 3\mu\theta^2(2\theta-3)\phi(\phi-1) \tag{4.7}$$

Figure 4.22 presents the preliminary results obtained with the introduction of variation in the ducts, a model defined by the Equations (3.18), (4.6) and (4.7).

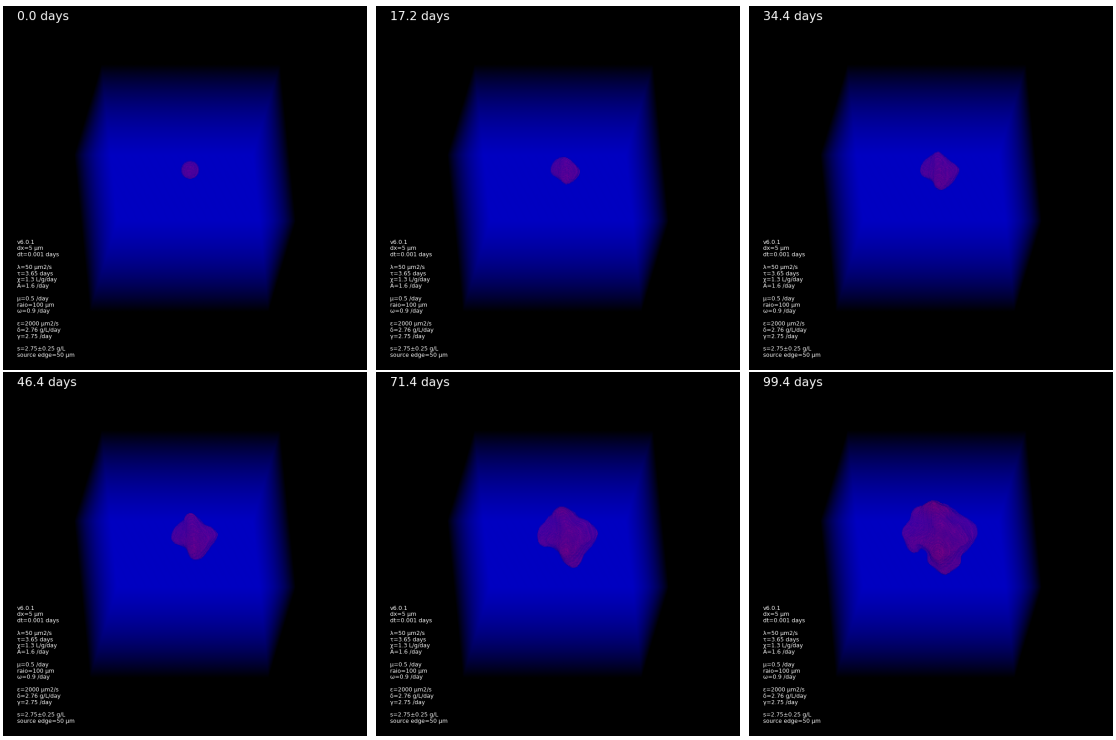

Figure 4.22: Simulation of tumor growth with ducts deformation.

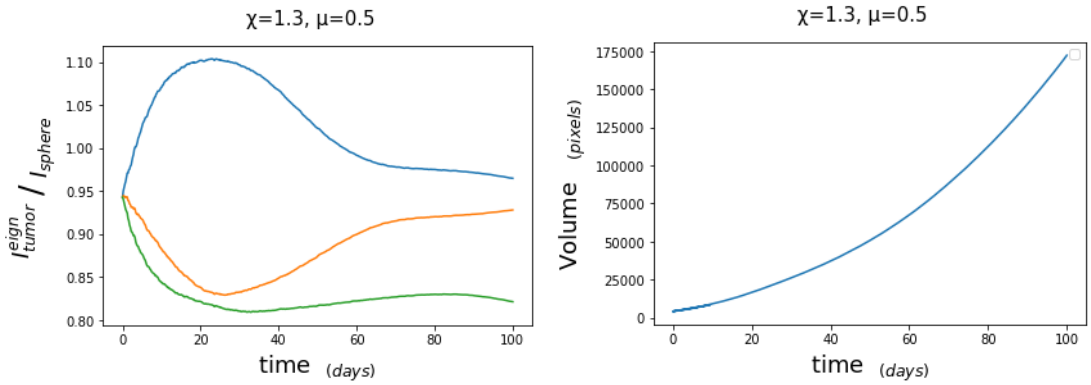

Figure 4.23: Moment of Inertia Ratio and Volume of the tumor in Figure 4.22. The 3 curves in the left plot correspond to each of the eigenvalues of the inertia tensor.

These results show the tumor growing almost as a sphere, with a slightly preferential growth over the ducts position. This is described by the Moment of Inertia Ratios shown in Figure 4.23. On the plot, one of the principal axes has a high ratio while the other two have lower ratios, this combination resembles a cylinder. However, the lower ratio axes still maintain a value above 0.8, meaning the tumor is not far from a spherical shape.

Chapter 5

Conclusion

With the models developed it was possible to study the first stages of PCa and the formation of some Gleason Patterns. Although both models developed can be improved further, several conclusions were extracted. Each model focused in a different approach to study PCa. The CPM allowed the study of cellular behavior and properties in a homeostatic environment and with tumor. The Phase-field model showed the influence of the ductal network in PCa.

5.1 Cellular Potts Model

A 2D CPM was developed to include the tubule-alveolar structure of the prostate, *Tumor* cells and *CSC*. The development of the model suggests that cellular death and proliferation can not be independent, otherwise the balance between luminal and basal layers would disappear, even with the same rate of proliferation and apoptosis. Implementing a paracrine signalling mechanism in the model created an homeostatic system. This suggests that cellular death may cause a signal to proliferation of *Stem* cells.

The simulations also suggest that the development of lower grade GP would only occur if the cells maintained a certain behavior, i.e., a polarization that cause the formation of underdeveloped structures, causing the cribriform pattern. At the same time, if the cells do not retain these characteristics, then higher grade GP would appear, namely the Solid GP5. With these observations, can be concluded that the accumulation of mutations as the tumor grows causes the cells to lose their normal behavior, becoming a more dangerous tumor, reflected by the GP.

The 2D model showed some limitations to recreate more diverse growth patterns. In the model, all tumor growth occurs in the same plane. However, slicing the structure created by the tumor growth in a 3D environment can cause the appearance of others GP (as seen in the

phase-field 3D model).

5.1.1 Future Work

There are 2 forms of improving the the CPM: add more components (e.g. oxygen) or add the 3rd dimension. Adding to the model oxygen or nutrients capable of influencing cellular death would allow for the formation of Solid GP5 with necrosis, which can not occur in the present model. It would also create conditions that facilitate directional growth of the tumor towards zones with higher concentrations of nutrients, like blood vessels.

A 3D model would allow to create a better representation of the prostate structure. It would be possible to analyze how the cells properties affect the tubuloalveolar structure and how this structure would be affected in PCa. A 3D model may allow to see the continuous lesions that originate different GP, as observed by Leenders *et al* [42].

5.2 Phase-field

A phase-field 3D model from [72] was adapted to include the microstructure of the prostate. From several methods tested, adding an energy term that decreases the energy inside the ducts proved to be the more stable method.

The model reacted to variations in proliferation and influence from the ducts. Proliferation affected tumor growth rate and the ducts played an important role in the patterns the tumor grows into. The ducts provided a path for the tumor to spread. If the tumor was not contained to the ducts, the simulation would reveal the formation of different GP in different zones of the simulation box, forming continuous patterns in space as described in [42]. The simulations suggest that the GP grades are influenced by the underlying structures and the time the tumor had to affect these structures (the closer to the starting point, the more deformed the structures are at the end of the simulation - higher grade GP).

5.2.1 Future Work

To differentiate between infiltration and deformation, the ductal network must change under the influence of the tumor. To improve the model, the ductal network (described by θ) must be dependent of the tumor, as attempted in subsection 4.2.4.

Bibliography

[1] International Agency for Research on Cancer. Cancer today. `https://gco.iarc.fr`, 2020. Accessed: 2021-07-04.

[2] Heide Schatten. Brief overview of prostate cancer statistics, grading, diagnosis and treatment strategies. *Cell & Molecular Biology of Prostate Cancer*, pages 1–14, 2018.

[3] Stacy Loeb, Marc A Bjurlin, Joseph Nicholson, Teuvo L Tammela, David F Penson, H Ballentine Carter, Peter Carroll, and Ruth Etzioni. Overdiagnosis and overtreatment of prostate cancer. *European urology*, 65(6):1046–1055, 2014.

[4] Kevin L Schwartz, Shabbir MH Alibhai, George Tomlinson, Gary Naglie, and Murray D Krahn. Continued undertreatment of older men with localized prostate cancer. *Urology*, 62(5):860–865, 2003.

[5] K-H Leissner and L-E Tisell. The weight of the human prostate. *Scandinavian journal of urology and nephrology*, 13(2):137–142, 1979.

[6] Barbara Young, Phillip Woodford, and Geraldine O'Dowd. *Wheater's Functional Histology Book: A Text and Colour Atlas*. Elsevier Health Sciences, 2013.

[7] Cancer Research UK. Diagram showing the position of the prostate and rectum. `https://commons.wikimedia.org/wiki/File:Diagram_showing_the_position_of_the_prostate_and_rectum_CRUK_358.svg`, 2014.

[8] Anil Bhavsar and Sadhna Verma. Anatomic imaging of the prostate. *BioMed research international*, 2014, 2014.

[9] J Frick and W Aulitzky. Physiology of the prostate. *Infection*, 19(3):S115–S118, 1991.

[10] John E McNeal. The zonal anatomy of the prostate. *The prostate*, 2(1):35–49, 1981.

[11] Christine H Lee, Oluyemi Akin-Olugbade, and Alexander Kirschenbaum. Overview of prostate anatomy, histology, and pathology. *Endocrinology and metabolism clinics of North America*, 40(3):565–75, 2011.

[12] John T Isaacs. Prostatic structure and function in relation to the etiology of prostatic cancer. *The Prostate*, 4(4):351–366, 1983.

[13] Barry G Timms. Prostate development: a historical perspective. *Differentiation*, 76(6):565–577, 2008.

[14] Vamsi Parimi, Rajen Goyal, Kate Poropatich, and Ximing J Yang. Neuroendocrine differentiation of prostate cancer: a review. *American journal of clinical and experimental urology*, 2(4):273, 2014.

[15] Alan J Wein, Louis R Kavoussi, Andrew C Novick, Alan W Partin, and Craig A Peters. *Campbell-Walsh urology: expert consult premium edition: enhanced online features and print, 4-volume set*. Elsevier Health Sciences, 2011.

[16] Geert JLH Van Leenders and Jack A Schalken. Epithelial cell differentiation in the human prostate epithelium: implications for the pathogenesis and therapy of prostate cancer. *Critical reviews in oncology/hematology*, 46:3–10, 2003.

[17] S Rizzo, G Attard, and DL Hudson. Prostate epithelial stem cells. *Cell Proliferation*, 38(6):363–374, 2005.

[18] John T Isaacs. Antagonistic effect of androgen on prostatic cell death. *The Prostate*, 5(5):545–557, 1984.

[19] Samuel R Denmeade, Xiaohui S Lin, and John T Isaacs. Role of programmed (apoptotic) cell death during the progression and therapy for prostate cancer. *The prostate*, 28(4):251–265, 1996.

[20] P Mao and A Angrist. The fine structure of the basal cell of human prostate. *Laboratory investigation; a journal of technical methods and pathology*, 15(11):1768–1782, 1966.

[21] Michel A Pontari, Geoffrey F Joyce, Matthew Wise, Mary McNaughton-Collins, and Urologic Diseases in America Project. Prostatitis. *The Journal of urology*, 177(6):2050–2057, 2007.

[22] Claus G Roehrborn. Benign prostatic hyperplasia: an overview. *Reviews in urology*, 7(Suppl 9):S3, 2005.

[23] Sabatino Ventura, Jocelyn N Pennefather, and Frederick Mitchelson. Cholinergic innervation and function in the prostate gland. *Pharmacology & therapeutics*, 94(1-2):93–112, 2002.

[24] Michael M Shen and Cory Abate-Shen. Molecular genetics of prostate cancer: new prospects for old challenges. *Genes & development*, 24(18):1967–2000, 2010.

[25] Henrik Grönberg. Prostate cancer epidemiology. *The Lancet*, 361(9360):859–864, 2003.

[26] Douglas W Strand and Andrew S Goldstein. The many ways to make a luminal cell and a prostate cancer cell. *Endocrine-Related Cancer*, 22(6):T187 – T197, 01 Dec. 2015.

[27] Raymond B Nagle, Frederick R Ahmann, Kathleen M McDaniel, Maria L Paquin, Virginia A Clark, and Abbie Celniker. Cytokeratin characterization of human prostatic carcinoma and its derived cell lines. *Cancer research*, 47(1):281–286, 1987.

[28] SH Lang, FM Frame, and AT Collins. Prostate cancer stem cells. *The Journal of Pathology*, 217(2):299–306, 2009.

[29] Anne T Collins and Norman J Maitland. Prostate cancer stem cells. *European journal of cancer*, 42(9):1213–1218, 2006.

[30] Shi-Ming Tu and Sue-Hwa Lin. Prostate cancer stem cells. *Clinical genitourinary cancer*, 10(2):69–76, 2012.

[31] Ricardo Leao, Celia Domingos, Arnaldo Figueiredo, Robert Hamilton, Uri Tabori, and Pedro Castelo-Branco. Cancer stem cells in prostate cancer: implications for targeted therapy. *Urologia internationalis*, 99(2):125–136, 2017.

[32] Vikram Narayan, Song Jiang, and Christopher A Warlick. Early stage cancer in older adults: Prostate—avoiding overtreatment and undertreatment. *The Cancer Journal*, 23(4):238–241, 2017.

[33] Richard M Hoffman. Screening for prostate cancer. *New England Journal of Medicine*, 365(21):2013–2019, 2011.

[34] Steven P Balk, Yoo-Joung Ko, and Glenn J Bubley. Biology of prostate-specific antigen. *Journal of clinical oncology*, 21(2):383–391, 2003.

[35] Donald F Gleason. Histologic grading of prostate cancer: a perspective. *Human pathology*, 23(3):273–279, 1992.

[36] Mark S Litwin and Hung-Jui Tan. The diagnosis and treatment of prostate cancer: a review. *Jama*, 317(24):2532–2542, 2017.

[37] DF Gleason. Veterans administration cooperative urological research group: Prediction of prognosis for prostatic adenocarcinoma by combined histologic grading and clinical staging. *J Urol*, 111:58–64, 1974.

[38] D Gleason. Histologic grading and clinical staging of carcinoma of the prostate. *Urologic pathology: the prostate*, 1977.

[39] National Institutes of Health. *morphology & grade. icd-o-3 morphology codes*. `https://commons.wikimedia.org/wiki/File:Gleasonscore.jpg`, 2021.

[40] Jonathan I Epstein, William C Allsbrook Jr, Mahul B Amin, Lars L Egevad, ISUP Grading Committee, et al. The 2005 international society of urological pathology (isup) consensus conference on gleason grading of prostatic carcinoma. *The American journal of surgical pathology*, 29(9):1228–1242, 2005.

[41] Ni Chen and Qiao Zhou. The evolving gleason grading system. *Chinese Journal of Cancer Research*, 28(1):58, 2016.

[42] Geert JLH van Leenders, Esther I Verhoef, and Eva Hollemans. Prostate cancer growth patterns beyond the gleason score: entering a new era of comprehensive tumour grading. *Histopathology*, 77(6):850–861, 2020.

[43] Esther I Verhoef, Wiggert A van Cappellen, Johan A Slotman, Gert-Jan Kremers, Patricia C Ewing-Graham, Adriaan B Houtsmuller, Martin E van Royen, and Geert JLH van Leenders. Three-dimensional architecture of common benign and precancerous prostate epithelial lesions. *Histopathology*, 74(7):1036–1044, 2019.

[44] Paul A Kay, Richard A Robb, and David G Bostwick. Prostate cancer microvessels: a novel method for three-dimensional reconstruction and analysis. *The Prostate*, 37(4):270–277, 1998.

[45] Eli Gibson, Mena Gaed, José A Gómez, Madeleine Moussa, Stephen Pautler, Joseph L Chin, Cathie Crukley, Glenn S Bauman, Aaron Fenster, and Aaron D Ward. 3d prostate

histology image reconstruction: Quantifying the impact of tissue deformation and histology section location. *Journal of pathology informatics*, 4, 2013.

[46] Paul A Kay, Richard A Robb, David G Bostwick, and Jon J Camp. Robust 3-d reconstruction and analysis of microstructures from serial histologic sections, with emphasis on microvessels in prostate cancer. In *International Conference on Visualization in Biomedical Computing*, pages 129–134. Springer, 1996.

[47] JP Michiel Sedelaar, Geert JLH van Leenders, Christian A Hulsbergen-van de Kaa, Henk G van der Poel, Jeroen AWM van der Laak, Frans MJ Debruyne, Hessel Wijkstra, and Jean JMCH de la Rosette. Microvessel density: correlation between contrast ultrasonography and histology of prostate cancer. *European urology*, 40(3):285–293, 2001.

[48] Eli Gibson, Mena Gaed, José A Gómez, Madeleine Moussa, Cesare Romagnoli, S Pautler, JL Chin, C Crukley, GS Bauman, A Fenster, et al. 3d prostate histology reconstruction: An evaluation of image-based and fiducial-based algorithms. *Medical physics*, 40(9):093501, 2013.

[49] Kang Cui, Xiangnan Li, Yabing Du, Xiance Tang, Seiji Arai, Yiwei Geng, Ying Xi, Han Xu, Yue Zhou, Wang Ma, et al. Chemoprevention of prostate cancer in men with high-grade prostatic intraepithelial neoplasia (hgpin): a systematic review and adjusted indirect treatment comparison. *Oncotarget*, 8(22):36674, 2017.

[50] Yuri Tolkach and Glen Kristiansen. Is high-grade prostatic intraepithelial neoplasia (hgpin) a reliable precursor for prostate carcinoma? implications for clonal evolution and early detection strategies. *The Journal of pathology*, 244(4):389–393, 2018.

[51] Lei Zhang, Yi Wang, Zhiqiang Qin, Xian Gao, Qianwei Xing, Ran Li, Wei Wang, Ninghong Song, and Wei Zhang. Correlation between prostatitis, benign prostatic hyperplasia and prostate cancer: A systematic review and meta-analysis. *Journal of Cancer*, 11(1):177, 2020.

[52] Guillermo Lorenzo, Thomas JR Hughes, Pablo Dominguez-Frojan, Alessandro Reali, and Hector Gomez. Computer simulations suggest that prostate enlargement due to benign prostatic hyperplasia mechanically impedes prostate cancer growth. *Proceedings of the National Academy of Sciences*, 116(4):1152–1161, 2019.

[53] Stephen J Freedland, William B Isaacs, Elizabeth A Platz, Martha K Terris, William J Aronson, Christopher L Amling, Joseph C Presti Jr, and Christopher J Kane. Prostate size and risk of high-grade, advanced prostate cancer and biochemical progression after radical prostatectomy: a search database study. *Journal of clinical oncology*, 23(30):7546–7554, 2005.

[54] Michael E Chen, Patricia Troncoso, Dennis Johnston, Kuang Tang, and R Joseph Babaian. Prostate cancer detection: relationship to prostate size. *Urology*, 53(4):764–768, 1999.

[55] Elisabeth G Rens and Leah Edelstein-Keshet. From energy to cellular forces in the cellular potts model: An algorithmic approach. *PLoS computational biology*, 15(12):e1007459, 2019.

[56] Alexander G Fletcher, Miriam Osterfield, Ruth E Baker, and Stanislav Y Shvartsman. Vertex models of epithelial morphogenesis. *Biophysical journal*, 106(11):2291–2304, 2014.

[57] François Graner and James A Glazier. Simulation of biological cell sorting using a two-dimensional extended potts model. *Physical review letters*, 69(13):2013, 1992.

[58] Tsuyoshi Hirashima, Elisabeth G Rens, and Roeland MH Merks. Cellular potts modeling of complex multicellular behaviors in tissue morphogenesis. *Development, growth & differentiation*, 59(5):329–339, 2017.

[59] Marco Scianna, Luigi Preziosi, and Katarina Wolf. A cellular potts model simulating cell migration on and in matrix environments. *Mathematical Biosciences & Engineering*, 10(1):235, 2013.

[60] András Szabó and Roeland MH Merks. Cellular potts modeling of tumor growth, tumor invasion, and tumor evolution. *Frontiers in oncology*, 3:87, 2013.

[61] Marco Scianna. An extended cellular potts model analyzing a wound healing assay. *Computers in biology and medicine*, 62:33–54, 2015.

[62] Thomas Thenard, Anita Catapano, Michel Mesnard, and Rachele Allena. A cellular potts energy-based approach to analyse the influence of the surface topography on single cell motility. *Journal of theoretical biology*, 509:110487, 2021.

[63] Joao Carvalho, Valeria Lopes, and Rui Travasso. Tumor cell invasiveness in the initial stages of bladder cancer development-a computational study. *International Journal for Numerical Methods in Biomedical Engineering*, 37(1):e3417, 2021.

[64] Roeland MH Merks, Erica D Perryn, Abbas Shirinifard, and James A Glazier. Contact-inhibited chemotaxis in de novo and sprouting blood-vessel growth. *PLoS Comput Biol*, 4(9):e1000163, 2008.

[65] Gervaise H Henry, Alicia Malewska, Diya B Joseph, Venkat S Malladi, Jeon Lee, Jose Torrealba, Ryan J Mauck, Jeffrey C Gahan, Ganesh V Raj, Claus G Roehrborn, et al. A cellular anatomy of the normal adult human prostate and prostatic urethra. *Cell reports*, 25(12):3530–3542, 2018.

[66] Rui DM Travasso, Mario Castro, and Joana CRE Oliveira. The phase-field model in tumor growth. *Philosophical Magazine*, 91(1):183–206, 2011.

[67] RS Qin and HK Bhadeshia. Phase field method. *Materials science and technology*, 26(7):803–811, 2010.

[68] Harald Garcke, Kei Fong Lam, and Andrea Signori. On a phase field model of cahn–hilliard type for tumour growth with mechanical effects. *Nonlinear Analysis: Real World Applications*, 57:103192, 2021.

[69] EABF Lima, JT Oden, DA Hormuth, TE Yankeelov, and RC Almeida. Selection, calibration, and validation of models of tumor growth. *Mathematical Models and Methods in Applied Sciences*, 26(12):2341–2368, 2016.

[70] Jiangping Xu, Guillermo Vilanova, and Hector Gomez. Phase-field model of vascular tumor growth: Three-dimensional geometry of the vascular network and integration with imaging data. *Computer Methods in Applied Mechanics and Engineering*, 359:112648, 2020.

[71] Pierluigi Colli, Hector Gomez, Guillermo Lorenzo, Gabriela Marinoschi, Alessandro Reali, and Elisabetta Rocca. Mathematical analysis and simulation study of a phase-field model of prostate cancer growth with chemotherapy and antiangiogenic therapy effects. *Mathematical Models and Methods in Applied Sciences*, 30(07):1253–1295, 2020.

[72] Guillermo Lorenzo, Michael A Scott, Kevin Tew, Thomas JR Hughes, Yongjie Jessica Zhang, Lei Liu, Guillermo Vilanova, and Hector Gomez. Tissue-scale, personalized modeling and simulation of prostate cancer growth. *Proceedings of the National Academy of Sciences*, 113(48):E7663–E7671, 2016.

[73] Tania Biswas and Elisabetta Rocca. Long time dynamics of a phase-field model of prostate cancer growth with chemotherapy and antiangiogenic therapy effects. *arXiv preprint arXiv:2010.11108*, 2020.

[74] Haym Kruglak. Achievement of physics students with and without laboratory work. *American Journal of Physics*, 21(1):14–16, 1953.

[75] Alex Brollo. Normal prostate. `https://commons.wikimedia.org/wiki/File:Prostate_normal_1.jpg`, 2005.

[76] Ben NG Giepmans and Sven CD van IJzendoorn. Epithelial cell–cell junctions and plasma membrane domains. *Biochimica et Biophysica Acta (BBA)-Biomembranes*, 1788(4):820–831, 2009.

[77] O Yu Ivanova, LB Margolis, Ju M Vasiliev, and IM Gelfand. Orientation of mitosis of fibroblasts is determined in the interphase. *Proceedings of the National Academy of Sciences*, 71(5):2032–2032, 1974.

[78] Nancy J Nesslinger, Robert A Sahota, Brad Stone, Kayli Johnson, Navraj Chima, Caitlin King, Devon Rasmussen, Darcy Bishop, Paul S Rennie, Martin Gleave, et al. Standard treatments induce antigen-specific immune responses in prostate cancer. *Clinical Cancer Research*, 13(5):1493–1502, 2007.

[79] Kenichiro Ishii, Shigeyuki Usui, Yoshiki Sugimura, Sei Yoshida, Takuichi Hioki, Masae Tatematsu, Hajime Yamamoto, and Kazuyuki Hirano. Aminopeptidase n regulated by zinc in human prostate participates in tumor cell invasion. *International journal of cancer*, 92(1):49–54, 2001.

Appendix A

Cellular Potts Model

A.1 Rule Set #1

Table A.1: Parameters used in the simulations from Figure 4.3. The target area and length is measured are pixels.

	Stroma	*Stem*	*Basal*	*Luminal*	*Lumen*
A_{target}	118583	55	56	166	20589
λ_a	1000	200	200	200	50
L_{target}	-	13	13	17	-
λ_l	0	200	200	200	0
P_{death}	-	-	-	0/0.1‰*	-

*Simulation A and B have 0 probability of death, while Simulation C has 0.1‰.

Table A.2: Value of adhesion energy between cell types used in the simulations from Figure 4.3.

	ECM	*Stroma*	*Stem*	*Basal*	*Luminal*	*Lumen*
Stroma	1.8	2.295	3.0	3.0	3.0	3.0
Stem	1.8	3.0	2.295	2.55	2.55	2.55
Basal	1.8	3.0	2.55	2.295	2.55	2.55
Luminal	1.8	3.0	2.55	2.55	2.295	2.55
Lumen	1.8	3.0	2.55	2.55	2.55	2.295

A.2 Rule Set #2

Stability Tests

Table A.3: Parameters used in the simulations from Figure 4.4-A and B. The target values are in pixels.

	Stroma	*Stem*	*Basal*	*Luminal*	*Lumen*
A_{target}	118583	55	56	166	20589
λ_v	1000	200/100*	200/100*	200/250*	50
L_{target}	-	13	13	17	-
λ_l	0	500	500	200	0
P_{death}	-	-	-	0	-

*The first value is used in Simulation A and the second in Simulation B

Table A.4: Parameters used in the simulations from Figure 4.4-C and D. The target values are in pixels.

	Stroma	*Stem*	*Basal*	*Luminal*	*Lumen*
A_{target}	118583	55	56	166	20589
λ_v	100/10000*	500	500	750/1000*	100
L_{target}	-	13	13	17	-
λ_l	0	750/1000*	750/1000*	500	0
P_{death}	-	-	-	0	-

*The first value is used in Simulation C and the second in Simulation D

Table A.5: Parameters used in the simulations from Figure 4.4-E and G. The target values are in pixels.

	Stroma	*Stem*	*Basal*	*Luminal*	*Lumen*
A_{target}	118583	55	56	166	20589
λ_v	1000	500	500	1000	100
L_{target}	-	13	13	17	-
λ_l	0	500	1000	500	0
P_{death}	-	-	-	0/0.2‰*	-

*The first value is used in Simulation E and the second in Simulation G

Table A.6: Parameters used in the simulations from Figure 4.4-F and H. The target values are in pixels.

	Stroma	*Stem*	*Basal*	*Luminal*	*Lumen*
A_{target}	118583	50	56	166	21000
λ_v	10000	500	500	1000	1
L_{target}	-	13	15	17	-
λ_l	0	1000	1000	500	0
P_{death}	-	-	-	0/0.1‰*	-

*The first value is used in Simulation F and the second in Simulation H

Table A.7: Value of adhesion energy between cell types used in the simulations from Figure 4.4.

	ECM	*Stroma*	*Stem*	*Basal*	*Luminal*	*Lumen*
Stroma	1.8	2.295	3.0	3.0	3.0	3.0
Stem	1.8	3.0	2.295	2.55	2.55	2.55
Basal	1.8	3.0	2.55	2.295	2.55/2.295*	2.55
Luminal	1.8	3.0	2.55	2.55/2.295*	2.295	2.55
Lumen	1.8	3.0	2.55	2.55	2.55	2.295

*The first value is used in Simulations A-F and the second value in Simulations G-H.

Tumor Growth

Table A.8: Parameters used in the simulations from Figure 4.5 and Figure 4.6. The target areas and lengths are in pixels.

	Stroma	*Stem*	*Basal*	*Luminal*	*Tumor*	*Lumen*
A_{target}	118583	50	56	166	166	21000
λ_a	10000	500	500	1000	1000	1
L_{target}	-	13	15	17	-	-
λ_l	0	1000	1000	500	0	0
P_{death}	-	-	-	0.1‰	0.1‰	-
$A_{mitosis}$	-	-	-	-	166	-

Table A.9: Value of adhesion energy between cell types used in the simulations from Figure 4.5 and Figure 4.6.

	ECM	*Stroma*	*Stem*	*Basal*	*Luminal*	*Tumor*	*Lumen*
Stroma	1.8	2.295	3.0	3.0	3.0	3.0	3.0
Stem	1.8	3.0	2.295	2.55	2.55	2.55	2.55
Basal	1.8	3.0	2.55	2.295	2.295	2.55	2.55
Luminal	1.8	3.0	2.55	2.295	2.295	2.295	2.55
Tumor	1.8	3.0	2.55	2.55	2.295	2.295	2.55
Lumen	1.8	3.0	2.55	2.55	2.55	2.55	2.295

Tumor Growth several shapes

Table A.10: Parameters used in the simulations from Figure 4.7. The target areas and lengths are in pixels.

	Stroma	*Stem*	*Basal*	*Luminal*	*Tumor*	*Lumen*
A_{target}	[1]	50/35[1][2]	56/40[1][2]	166/147[1][2]	166/150[1][2]	[1]
λ_a	10000	500	500	1000	1000	1
L_{target}	-	13/11[1][2]	15/13[1][2]	17/21[1][2]	-	-
λ_l	0	1000	1000	500	0	0
P_{death}	-	-	-	0.1‰	0.1‰	-
$A_{mitosis}$	-	-	-	-	166/200[2]	-

[1] The target values are the average values in the initial moment, varying between all simulations.

[2] The second value is the one used in the simulation of the last row.

Table A.11: Value of adhesion energy between cell types used in the simulations from Figure 4.7.

	ECM	*Stroma*	*Stem*	*Basal*	*Luminal*	*Tumor*	*Lumen*
Stroma	1.8	2.295	2.3	2.3	5.0/10[1]	3.0	3.0
Stem	1.8	2.3	2.4	2.4	2.295	2.55	2.55
Basal	1.8	2.3	2.4	2.4	2.295/1.0[1]	2.55/1.0[1]	2.55
Luminal	1.8	5.0/10[1]	2.295	2.295/1.0[1]	2.4	2.295/2.4[1]	2.55
Tumor	1.8	3.0	2.55	2.55/1.0[1]	2.295/2.4[1]	2.295/3.0[1]	2.55
Lumen	1.8	3.0	2.55	2.55	2.55	2.55	2.295

[1] The second value is the one used in the simulation of the last row.

A.3 Rule Set #3

Table A.12: Parameters used in the simulations from Figure 4.8. The target area and lengths are in pixels.

	Stroma	*Stem*	*Basal*	*Luminal*	*Tumor*	*Lumen*
A_{target}	-	57	57	183	190	8161
λ_a	0	500	500	1000	1000	10000
L_{target}	-	14	14	18	18	-
λ_l	0	1000	1000	500	1000	0
P_{death}	-	-	-	0.13‰	0.13‰	-
$A_{mitosis}$	-	-	-	-	190	-

Table A.13: Value of adhesion energy between cell types used in the simulations from Figure 4.8.

	ECM	*Stroma*	*Stem*	*Basal*	*Luminal*	*Tumor*	*Lumen*
Stroma	1.8	2.295	1.0	1.0	10.0	10.0	10.0
Stem	1.8	1.0	1.1	1.1	1.2	1.2	10.0
Basal	1.8	1.0	1.1	1.1	1.2	1.2	3.0
Luminal	1.8	10.0	1.2	1.2	2.4	2.4	2.55
Tumor	1.8	10.0	1.2	1.2	2.4	2.5	2.55
Lumen	1.8	10.0	10.0	3.0	2.55	2.55	3.0

A.4 Rule Set #4

Table A.14: Parameters used in the simulations from Figure 4.9. The target area and lengths are in pixels.

	Stroma	*Stem*	*Basal*	*Luminal*	*Tumor*	*CSC*	*Lumen*
A_{target}	-	54	55	91	91	60	2801
λ_a	0	500	500	1000	1000	1000	5000
L_{target}	-	11	11	13	13	11	-
λ_l	0	1000	1000	500	1000	500	0
P_{death}	-	-	-	0.13‰	0.13‰	-	-
$A_{mitosis}$	-	-	-	-	91	60	-

Table A.15: Value of adhesion energy between cell types used in the simulations from Figure 4.9.

	ECM	*Stroma*	*Stem*	*Basal*	*Luminal*	*Tumor*	*CSC*	*Lumen*
Stroma	1.8	2.295	1.2	1.2	10.0	10.0	1.0	10.0
Stem	1.8	1.2	1.2	1.2	1.3	1.2	1.2	10.0
Basal	1.8	1.2	1.2	1.2	1.2	1.2	1.2	3.0
Luminal	1.8	10.0	1.3	1.2	2.4	2.4	2.4	2.55
Tumor	1.8	10.0	1.2	1.2	2.4	2.5	1.2	2.55
CSC	1.8	1.0	1.2	1.2	2.4	1.2	10.0	10.0
Lumen	1.8	10.0	10.0	3.0	2.55	2.55	10.0	0.0